Revision 2
Word Count: 9853 (including title, abstract, references, figure captions)

The $^{34}S/^{32}S$ homogeneity of Chemical Vapor Transport (CVT) Reaction-synthesized pyrites

LI LIU[1,2,1] , BIN FU[3], XING DING[1,2], JING GU[4]
[1]State Key Laboratory of Isotope Geochemistry, Guangzhou Institute of Geochemistry, Chinese Academy of Sciences, Guangzhou 510640, China
[2]CAS Center for Excellence in Deep Earth Science, Guangzhou 510640, China.
[3]Research School of Earth Sciences, The Australian National University, Canberra, Australian Capital Territory 2601, Australia
[4]State Key Laboratory of Ore Deposit Geochemistry, Institute of Geochemistry, Chinese Academy of Sciences, Guiyang 550081, China

ABSTRACT

Chemical Vapor Transport (CVT) Reaction is an important and efficient method of synthesizing pyrite crystals. CVT-grown pyrites have been comprehensively investigated for physical properties and elemental chemical compositions. However, the isotopic compositions have not been paid attention. In this study, four series of pyrite crystals (PY3, PY4, PY5, PY6) were synthesized using CVT method, with PY5 undoped and the others doped with nickel. The synthesized crystals were characterized qualitatively with confocal laser Raman microspectroscopy and quantitatively by EMPA, LA-ICPMS, SIMS, and IRMS. The synthetic products are irregular polycrystalline aggregates or cubic and octahedral monocrystals, with characteristic Raman bands at ~344 cm^{-1}, ~380 cm^{-1}/377 cm^{-1}, ~427 cm^{-1}/430 cm^{-1}, and S/Fe weight and atomic ratios of 1.15–1.17 and 2.01–2.04 respectively indicative of pyrite. The pyrites contain traces of inevitable impurities such as Si and Br. The nickel contents of Ni-doped pyrites are heterogeneous, 39–27300 ppm for PY3, 24–21700 ppm for PY4, and 57–2610 ppm for PY6. By comparison, the $\delta^{34}S$ values obtained by SIMS are relatively homogeneous (PY3 = 17.3 ± 0.9‰, PY4 = 17.7 ± 0.8‰, PY5 = 17.9 ± 0.8‰, PY6 = 17.7 ± 0.6‰, ±2SD), and are consistent with IRMS $\delta^{34}S$ values (17.8 ± 0.2‰ for PY3, 18.3 ± 0.9‰ for PY4, 18.2 ± 0.3‰ for PY5, 18.1 ± 0.1‰ for PY6, ±2SD). The homogeneity of $^{34}S/^{32}S$ suggests that CVT has the potential to synthesize reference materials for the determination of sulfur isotopic composition of pyrite using in-situ techniques. Additionally, we also investigated the matrix effects of nickel in pyrite on the measurement of $^{34}S/^{32}S$ by SIMS, and a preliminary equation of $\Delta^{34}S$ (‰) = $-0.59 \times Ni(wt\%)^{0.27}$ was derived for calibration.

Keywords: CVT reaction, pyrite, $^{34}S/^{32}S$, nickel, matrix effects, SIMS

[1] E-mail: emmaliu1016@gmail.com

This is the peer-reviewed, final accepted version for American Mineralogist, published by the Mineralogical Society of America.
The published version is subject to change. Cite as Authors (Year) Title. American Mineralogist, in press.
DOI: https://doi.org/10.2138/am-2023-9029. http://www.minsocam.org/

INTRODUCTION

Natural pyrite (FeS_2) is extremely abundant on the Earth. They are widespread in sediments, (meta-)sedimentary rocks and hydrothermal deposits (Rickard, 2012). However, due to the common occurrences of impurities (e.g., Ni, As, Co, Se, etc.), they cannot be used for certain purposes, for instance, semiconductor with a special requirement of electrical properties. In such cases, pure pyrite or pyrite doped with a specific element needs to be synthesized in the laboratory. Pyrite crystals can be synthesized in high-temperature solid-state (Clark, 1960; Fiechter et al., 1986) or wet-chemical (Xian et al., 2016 and references therein) ways. Chemical Vapor Transport (CVT) Reaction is a solid-state method that has been long and widely applied to synthesizing undoped or specific element-doped pyrite with the use of halogen compound(s) such as $AlCl_3$, KCl, $AlBr_3$, $FeBr_3$ as transport agents (Lehner et al., 2006; Diener and Köppe, 2012; Lehner et al., 2012). CVT-grown pyrite is well crystallized and the monocrystals can be up to millimeters in size. In addition, the crystals are pure FeS_2 without other iron sulfide phases.

The optical, electronic, and electrical properties (e.g., resistivity/resistance, carrier concentration, Hall coefficient, Hall mobility) of CVT-synthesized pyrite crystals have been investigated comprehensively for the purposes of, for instance, revealing the causes of low open-circuit voltages (Voigt et al., 2020), confirming the surface conduction (Walter et al., 2017), exploring the effects of dopants (Lehner et al., 2006; Lehner et al., 2012). In comparison, their chemical compositions have not been paid much attention, with the exception of the concentrations of (unintentional) doped impurities, which have been measured using Secondary Ion Mass Spectrometry (SIMS), Electron Probe Micro-analyzer (EPMA), Laser Ablation-Inductively Coupled Plasma Mass Spectrometry (LA-ICPMS), Rutherford Backscattering, ICPMS, Inductively Coupled Plasma Atomic Emission Spectrometry (ICPAES), and Proton Induced X-ray Emission (PIXE) to establish the relationship between impurities and electrical properties (Lehner et al., 2006; Lehner et al., 2012). The isotopic compositions, nevertheless, have not been examined yet.

Reference materials are critical for in-situ analytical methodology such as SIMS and LA-ICPMS. Current reference materials for the in-situ determination of pyrite sulfur isotopic composition are all of natural origin, e.g., Ruttan pyrite, Balmat pyrite (Crowe and Vaughan, 1996; Ireland et al., 2014), Sierra pyrite (LaFlamme et al., 2016), Sonora

pyrite (Farquhar et al., 2013; Chen et al., 2015), Maine pyrite (Philippot et al., 2007; Muller et al., 2017; Philippot et al., 2018), PPP-1 pyrite (Li et al., 2017; Li et al., 2018; Li et al., 2021), and Py-1 pyrite (Li et al., 2021). The main problem with natural reference materials is the limited quantity. With the rapid increase in the application of in-situ analysis, accelerated consumption of the reference materials can be expected. As a consequence, seeking and developing new reference materials will be needed. Recently, some pioneering work (e.g., Feng et al., 2022) has been conducted to artificially synthesize sulfide reference materials in the laboratory for LA-MC-ICP-MS analysis using high-temperature melting and plasma-activated sintering, which provides an alternative way to develop reference materials for in-situ analysis. CVT-grown pyrite crystals, with their moderate to large sizes, have the potential to act as reference materials, provided that the composition is homogeneous.

This study synthesized undoped and nickel-doped pyrite crystals via CVT reactions. We measured the $^{34}S/^{32}S$ of these crystals in situ using SIMS (SHRIMP-SI) and the concentration of nickel in situ using EPMA and LA-ICPMS to examine the distribution of sulfur isotopes and doped trace element. By these investigations, we aim to assess whether CVT-synthesized pyrite crystals have the potential to be used as reference materials.

METHODS

Experimental

The pyrites were synthesized using Chemical Vapor Transport (CVT) Reaction method described in Lehner et al. (2006). Four series of pyrite crystals were synthesized (PY3, PY4, PY5, and PY6) from four experiments at the Guangzhou Institute of Geochemistry, Chinese Academy of Sciences (GIGCAS).

For the synthesis of PY4, PY5, and PY6, purchased FeS (99.9%, Macklin) was well mixed with sulfur (99.999%, damas-beta) and nickel (99.9%, Macklin) powder in a clean mortar, with a $(FeS/S)_{molar}$ ratio of approximately 5/4 following Lehner et al. (2006). A small amount of $FeBr_3$ powder (99%, Adamas) was rapidly loaded into a clean silica glass tube (6-mm ID, 10-mm OD; cleaned using ethanol, HCl, and deionized water; dried in an oven at 110 °C), and the FeS-S-Ni mixture was then loaded onto $FeBr_3$. The glass tube was subsequently evacuated, and sealed using a torch, resulting in a length of 12 cm (in adjustment to the temperature gradient of the horizontal furnace). The tube was placed in a rapid-quench pressure vessel, which was heated in a horizontal furnace for 14 to 15 days with a temperature of ~650 °C at the hot end and ~550 °C at the cold end (a gradient of ~100 °C); the pressure was around 3–11 MPa (Argon gas as pressure medium). The temperature was monitored using a K-type thermocouple. After the experiments, the tube

was quenched within several seconds by pulling out and tilting the pressure vessel.

For the synthesis of PY3, FeS was synthesized in the laboratory with starting materials of iron (99.9%, Macklin) and sulfur (99.999%, damas-beta). An equimolar mixture of iron and sulfur was loaded into a clean silica glass tube. A silica glass rod (3 mm in diameter, 4 cm in length, cleaned and dried) was loaded onto the mixture. The glass tube was then evacuated and sealed, and subsequently was heated to 600 °C and held for 14 days, with a low pressure of around 3 MPa (Argon gas as pressure medium).

Analytical_confocal laser Raman microspectroscopy

The Raman spectroscopic analysis was conducted at GIGCAS. The analyses were performed on recovered crystals. The Raman spectra were obtained using a high-resolution confocal Raman microscope WITec alpha300 R system equipped with a frequency doubled Nd:YAG laser emitting at 532 nm (fiber-coupled). A Zeiss 50 × objective was used to focus the laser onto an approximately 1-μm spot. A diffraction grating of 300 g/mm was used to disperse the light. The spectrometer was equipped with a back-illuminated CCD camera. Single spectrum acquisition mode was used. The surface laser power was 6–10 mW. A pure silicon wafer (111) (520 cm^{-1}) was used to calibrate the spectra before the analysis of experimental products. The scan range was 100–4000 cm^{-1}. In order to optimize the spectra and obtain sufficient signal-to-noise ratio to characterize the solid phases, 10 accumulations of 1-second integration were conducted. The obtained raw Raman spectra were processed with cosmic ray removal and background subtraction.

Analytical_electron microscopy

The synthesized crystals were selected under a binocular microscope and cast in 25-mm epoxy mounts together with Ruttan pyrite and Balmat pyrite (reference materials for SIMS analyses), and were then ground and polished to expose the mid-planes of most grains.

Back-scattered electron (BSE) imaging was conducted using a JEOL JSM6610A Analytical SEM (Scanning Electron Microscope) at the Research School of Earth Sciences (RSES), The Australian National University (ANU). The instrument was operated at 15 kV with images obtained at a loading current of ca. 50 μA with working distance of 10 mm.

Chemical compositions of these synthesized crystals were measured using a JEOL 8530F Plus electron probe micro-analyzer (EPMA) equipped with five wavelength-dispersive spectrometers and a Schottky Field Emission (FE) gun at the Centre for Advanced Microscopy (CAM), ANU. The analytical conditions were 15 kV

This is the peer-reviewed, final accepted version for American Mineralogist, published by the Mineralogical Society of America.
The published version is subject to change. Cite as Authors (Year) Title. American Mineralogist, in press.
DOI: https://doi.org/10.2138/am-2023-9029. http://www.minsocam.org/

(acceleration voltage), 30 nA (beam current), and 20 μm (spot size). Counting times were 10 seconds (peak and background) for major elements and 50 or 60 seconds for trace elements. Calibrations were made using synthetic and natural ASTIMEX mineral and metal standards: Si (sanidine) (*Crystal: TAP*), Br (TlBrI) (*Crystal:* TAPL), S (pyrite), Cl (Tugtupite) (*Crystal:* PETL), Fe (pyrite), Ni (pentlandite) (*Crystal:* LIFL). Limits of detection were typically 20 to 150 ppm. Data were processed using full ZAF corrections.

Analytical_laser ablation ICP-MS

Trace element abundances were determined using a 193 nm wavelength excimer laser (110 ArF Coherent COMPexPro, Lambda Physik) based "HelEx" ablation system equipped with an Agilent Technologies 7700 quadrupole inductively coupled plasma mass spectrometer (ICP-MS) (Eggins et al., 2005) at RSES, ANU. The sampling cell was a "HelEx" two-volume vortex cell in an atmosphere of Ar and He. The laser spot size was 28 μm in diameter. Data acquisition involved a 20-second background measurement followed by 45 seconds of ablation, with a repetition rate of 5 Hz and laser energy of 80 mJ. Dwell times on each isotope are 0.01 to 0.05 second, totaling about 0.28 second for each mass sweep. In addition to the doped element nickel, other trace elements were also measured; silicon was analyzed to detect whether there are contaminations by the silica glass tube, bromine was measured to investigate whether or not there is bromine involvement in the products via the transport agent $FeBr_3$. The following masses were measured: ^{29}Si, ^{34}S, ^{35}Cl, ^{49}Ti, ^{53}Cr, ^{57}Fe, ^{59}Co, ^{60}Ni, ^{77}Se, and ^{79}Br. Data were reduced and signals were integrated offline using the software package Iolite (e.g., Hellstrom et al., 2008; Paton et al., 2010, 2011). The results were calibrated against MASS1 with Fe determined by EPMA as the internal standard. Other reference materials including NIST SRM 610, 612 and BCR2G synthetic glasses (Jochum et al., 2005, 2011; Marks et al., 2016 and references therein), BB1, BB2 and SY scapolites (Kendrick, 2012), STDGL3 (Steadman et al., 2020), Ruttan and Balmat pyrites were also measured as monitors for data quality control.

Analytical_SIMS

Sulfur isotopic compositions ($^{34}S/^{32}S$) of the synthesized crystals were measured on SHRIMP-SI (Sensitive High Resolution Ion Microprobe - Stable Isotope) at RSES, ANU. The mounts were thoroughly cleaned and dried before being gold-coated and loaded onto the outer rack of source chamber.

A 15 keV primary Cs^+ ion beam emitted by a Kimball Physics IGS4 ion gun was utilized to sputter the sample (spot size was approximately 30 × 27 μm), resulting in negative secondary ions of 10 keV. Electron gun was not used. The secondary sulfur ions

This is the peer-reviewed, final accepted version for American Mineralogist, published by the Mineralogical Society of America.
The published version is subject to change. Cite as Authors (Year) Title. American Mineralogist, in press.
DOI: https://doi.org/10.2138/am-2023-9029. http://www.minsocam.org/

were focused to the source slit (60 μm in width) through ion extraction system, and were then transferred through the mass analyzer to the collector. $^{32}S^-$ and $^{34}S^-$ were collected simultaneously by Faraday cups, and were measured using current mode with resistors of 10^{12} Ω.

All the measurements were carried out in a single session. Analyses of reference materials Ruttan pyrite (primary, $\delta^{34}S_{V\text{-}CDT}$ = 1.2 ± 0.1‰; Crowe and Vaughan, 1996) and Balmat pyrite (secondary, $\delta^{34}S_{V\text{-}CDT}$ = 15.1 ± 0.2‰; Crowe and Vaughan, 1996) were performed typically after every three to five unknowns to correct for instrumental mass fractionation (IMF). Each spot analysis comprised one set, with each set composed of six scans and each scan consisting of ten subcounts of two-second integration. To investigate the effects of Ni and Cu in pyrite on the determination of $^{34}S/^{32}S$, we also measured Norilsk pentlandite and chalcopyrite with bulk $\delta^{34}S_{V\text{-}CDT}$ values of 7.9 ± 0.2‰ and 8.0 ± 0.2‰, respectively (Crowe and Vaughan, 1996).

All the data of unknowns were calibrated against Ruttan pyrite. The measured $^{34}S^-/^{32}S^-$ ratios are expressed in delta notation as per mil deviations from the standard ratios of Vienna-Canyon Diablo Troilite (V-CDT): $\delta^{34}S_{V\text{-}CDT}$ (‰) = $[(^{34}S/^{32}S)_{unknown}/(^{34}S/^{32}S)_{V\text{-}CDT} - 1] \times 1000$, where $(^{34}S/^{32}S)_{unknown}$ and $(^{34}S/^{32}S)_{V\text{-}CDT}$ are the $^{34}S/^{32}S$ ratios of the unknown and V-CDT, respectively. The internal error of each spot analysis is calculated as $1000 \times 2SE_{unknown}/(^{34}S/^{32}S)_{V\text{-}CDT}$, where $(^{34}S/^{32}S)_{V\text{-}CDT}$ is 0.044162589 (Ding et al., 2001) and $2SE_{unknown}$ is two standard error of the $^{34}S/^{32}S$ ratio of unknown. The external error was calculated following $[(1000 \times 2SE_{unknown}/(^{34}S/^{32}S)_{V\text{-}CDT})^2 + (1000 \times 2SE_{Ruttan}/(^{34}S/^{32}S)_{V\text{-}CDT})^2]^{0.5}$, where $2SE_{Ruttan}$ is two standard error of the $^{34}S/^{32}S$ ratio of Ruttan pyrite.

Analytical_isotope ratio mass spectrometry (IRMS)

The bulk sulfide isotopic composition analyses were conducted at the Institute of Geochemistry, Chinese Academy of Sciences. Sulfide powder with about 50 μg sulfur was weighed into a tin capsule, which was then put into a reaction vessel filled with oxidant WO_3 and reductant copper. Oxygen was pumped in simultaneously. With the reaction vessel rich in pure oxygen, sulfide and tin were combusted rapidly, producing SO_2 and SO_3. SO_3 was reduced to SO_2 by copper; SO_2 was then introduced into mass spectrometer in a He gas flow for sulfur isotope analysis. The sulfur isotopic compositions were measured using a MAT253 continuous flow Isotope Ratio Mass Spectrometer (Thermo Finnigan) coupled to a Flash EA 2000 Elemental Analyzer. The precision and accuracy were monitored by three IAEA reference materials (Ag_2S): IAEA-S-1 ($\delta^{34}S_{V\text{-}CDT}$ = −0.3‰), IAEA-S-2 ($\delta^{34}S_{V\text{-}CDT}$ = 22.6‰), and IAEA-S-3 ($\delta^{34}S_{V\text{-}CDT}$ = −32.5‰).

This is the peer-reviewed, final accepted version for American Mineralogist, published by the Mineralogical Society of America.
The published version is subject to change. Cite as Authors (Year) Title. American Mineralogist, in press.
DOI: https://doi.org/10.2138/am-2023-9029. http://www.minsocam.org/

RESULTS

After the rapid quench of each experiment, pale-yellow crystals were observed at the low-temperature end of the recovered silica glass tube. Portions of the crystals were adhered to the tube walls whereas the others were movable. The majority of the products are polycrystalline, approximately 2–5 mm in size (Fig. 1); the monocrystals are much smaller cubes, octahedra, etc. The Ni-doped crystals show better crystallization than the undoped ones, and are mostly euhedral (Fig. 1).

Raman spectra

The Raman spectra of the synthesized crystals show bands at ~344 cm^{-1}, ~380 cm^{-1} or 377 cm^{-1}, ~427 cm^{-1} or 430 cm^{-1} (Fig. 2). In most spectra, the strongest peaks are at ~380 cm^{-1}/377 cm^{-1}, and then ~344 cm^{-1}, while the bands at ~427 cm^{-1}/430 cm^{-1} have the lowest intensity (Fig. 2).

Major elements

The contents of major elements in the products are summarized in Table 1, and all the detailed EPMA data are presented in Supplementary Table 1. The S/Fe weight and atomic ratios of PY3 (1.17 ± 0.03, 2.04 ± 0.06, ±2SD), PY4 (1.16 ± 0.02, 2.02 ± 0.04), PY5 (1.15 ± 0.01, 2.01 ± 0.02), and PY6 (1.16 ± 0.01, 2.02 ± 0.02) are close to those of Ruttan pyrite (1.16 ± 0.01, 2.01 ± 0.02) and Balmat pyrite (1.16 ± 0.01, 2.01 ± 0.02). PY5 (undoped), Ruttan pyrite, and Balmat pyrite contain no nickel. PY3 contain the most nickel (0.44 ± 1.18 wt%), followed by PY4 (0.18 ± 0.89 wt%) and PY6 (0.12 ± 0.17 wt%). The Ni concentrations vary among different crystals, 0–2.42 wt% in PY3, 0–2.29 wt% in PY4, and 0–0.36 wt% in PY6; within a single crystal, the range is 0.02–0.48 wt% in PY4, 0.02–1.71 wt% in PY3, and 0.05–0.31 wt% in PY6. The Si, Br, Cl contents in PY3, PY4, PY5, and PY6 determined by EPMA are 0.

Trace elements

The raw data were calibrated against MASS1 for the concentrations of Ni, Cr, Co, Se, and NIST SRM 610 for the contents of Si, Ti, Br, Cl. The trace element concentrations in the products are summarized in Table 2, and all the data are presented in Supplementary Table 2. The MASS1-calibrated concentrations of Ni, Cr, Co, Se for the secondary reference materials STDGL3 and BCR2G are in good accordance with the referenced values (Supplementary Table 2, note that there is no referenced value of Cr for STDGL3, and Se for BCR2G), for instance, the measured Ni concentrations of STDGL3 are 216 to

232 ppm with referenced value of 247 ppm, and the measured Ni abundances of BCR2G are 11 to 12 ppm with referenced value of 13 ppm. The NIST SRM 610-calibrated Ti and Si concentrations of the secondary reference materials agree well with the referenced values (Supplementary Table 2). For Br and Cl, however, there are slight discrepancies. The Br contents in BCR2G are approximately consistent with the referenced values, whereas the Cl concentrations are higher (289 to 401 ppm vs. 98 ppm/67 ppm). For SY, the measured Br abundances range from 1400 to 4200 ppm, higher than the referenced value of 883 ppm; the measured Cl concentrations are one order of magnitude lower than the referenced value. The discrepancies in BB1a are similar.

Silicon is the dominant trace element in both Ruttan pyrite and Balmat pyrite. Ruttan pyrite also contains a small amount of Co, Cl, Ti, Se, and negligible Ni; Balmat pyrite has slight Cl, Ti, Ni, and Co (Table 2; Supplementary Table 2). In the synthesized crystals, silicon is a widespread impurity with relatively constant abundances of 200 to 500 ppm. Other impurities, including Br, Cl, Ti, Cr, Co, are low in concentration, with the exception of several analyses showing slightly higher contents of Br. The dopant Ni is the main trace element in products, except for PY5 that are undoped. The results show significant variations in Ni abundances in both inter- and intra-grains of PY3, PY4, and PY6. The Ni concentration ranges from 39 to 27300 ppm in different PY3 grains, 24 to 21700 ppm in PY4 grains, and 57 to 2610 ppm in PY6 grains, respectively. The intra-grain ranges of Ni contents in PY3 grains are 7510–27300 ppm, 387–601 ppm, 3000–8860 ppm, 39–164 ppm, 1815–3550 ppm, 1373–2350 ppm, 228–365 ppm, and 596–1216 ppm; those in PY4 grains are 63–509 ppm, 177–439 ppm, 296–450 ppm, 199–316 ppm, 1286–2930 ppm, 656–729 ppm, and 463–475 ppm; those in PY6 grains are 1148–1840 ppm, 310–753 ppm, 57–426 ppm, 355–1772 ppm, 995–2610 ppm, 1450–2020 ppm, and 622–1280 ppm. EPMA-derived Ni contents and LA-ICPMS-obtained Ni concentrations are in good accordance (Fig. 3).

Sulfur isotopic composition_SIMS

The count rates (counts per second, CPS) of $^{32}S^-$ and $^{34}S^-$ are 0.9–1.4 GHz and 40–60 MHz, respectively. The 45 analyses of Ruttan pyrite yield a mean $\delta^{34}S$ value of 1.2 ± 0.6‰ (2SD), and the 10 analyses of Balmat pyrite have a mean $\delta^{34}S$ value of 15.4 ± 0.7‰ (2SD). The internal error and external error (2σ) of $\delta^{34}S$ for each spot analysis range from 0.1 to 0.6 ‰ and 0.6 to 0.9 ‰, respectively.

The SIMS sulfur isotope data are summarized in Table 3, and all the data are listed in Supplementary Table 3. The 26 spot analyses performed on 11 different PY3 grains show $\delta^{34}S$ values of 16.2 to 18.2‰, averaging at 17.3‰ (2SD = ±0.9‰) (Fig. 4). The $\delta^{34}S$ ranges of the eight grains with multiple analyses are 16.2–17.6‰, 16.5–17.7‰, 16.7–17.4‰, 16.9–18.0‰, 17.1–17.7‰, 17.4–18.2‰, 17.2–17.8‰, and 17.4–17.5‰, respectively. The

26 spot analyses on 14 different PY4 crystals exhibit $\delta^{34}S$ values ranging from 17.0 to 18.7‰, yielding a mean of 17.7‰ (2SD = ±0.8‰) (Fig. 4). The seven monocrystals with multiple analyses show $\delta^{34}S$ values varying from 17.2 to 18.4‰, 17.5 to 17.6‰, 17.0 to 17.8‰, 17.5 to 17.6‰, 17.7 to 18.2‰, 18.0 to 18.7‰, and 17.4 to 17.7‰, respectively. The 32 spot analyses conducted on 14 PY5 crystals display $\delta^{34}S$ values of 16.6 to 18.7‰, with a mean of 17.9‰ (2SD = ±0.8‰) (Fig. 4). The eight single grains show $\delta^{34}S$ values ranging from 18.1 to 18.7‰, 16.6 to 18.1‰, 17.4 to 17.7‰, 17.2 to 18.2‰, 17.4 to 18.2‰, 17.9 to 18.0‰, 17.7 to 18.2‰, and 17.8 to 18.1‰, respectively. The 22 spot analyses on eight PY6 grains show $\delta^{34}S$ values varying from17.0 to 18.4 ‰, yielding a mean of 17.7‰ (2SD = ±0.6‰) (Fig. 4). The $\delta^{34}S$ variations of the seven monocrystals are 17.8–18.0‰, 17.0–17.9‰, 17.7–18.0‰, 17.4–18.1‰, 17.3–17.6‰, 17.9–18.4‰, and 17.3–18.0‰, respectively. The Norilsk pentlandite shows $\delta^{34}S$ values (calibrated to Ruttan pyrite) of 6.2 to 7.1‰ with a mean of 6.6 ± 0.6‰ (2SD), thus an average discrepancy of −1.3‰ compared with the bulk $\delta^{34}S$ value (7.9 ± 0.2‰, Crowe and Vaughan, 1996). The Ruttan pyrite-calibrated $\delta^{34}S$ values of Norilsk chalcopyrite range from 8.1 to 9.1‰, averaging at 8.5‰ (2SD = ±0.5‰). Compared with the bulk $\delta^{34}S$ value of 8.0 ± 0.2‰ (Crowe and Vaughan, 1996), the average bias is 0.5‰.

Sulfur isotopic composition_IRMS

All data were reported in standard delta notation ($\delta^{34}S$) relative to V-CDT. The precision is better than 0.2‰ (1σ). The three aliquots of PY3, PY5, and the two aliquots of PY6 show relatively consistent sulfur isotopic compositions, with $\delta^{34}S$ values of 17.8 ± 0.2‰ (2SD), 18.2 ± 0.3‰, and 18.1 ± 0.1‰, respectively (Table 4). The products of PY4 exhibit slight dispersion, with $\delta^{34}S$ values ranging from 17.9‰ to 18.8‰ (18.3 ± 0.9‰) (Table 4).

DISCUSSION

Products

Compositionally, the products have S/Fe weight and atomic ratios of 1.15–1.17 and 2.01–2.04, respectively (Table 1), similar to that of natural Ruttan pyrite (1.16, 2.01) and Balmat pyrite (1.16, 2.01), corresponding to a chemical formula of FeS_2 (ideal S/Fe ratio of 2 and weight ratio of 1.15). The slight deviations can be attributed to the impurities/trace elements substitutions for Fe and S, including Ni, Si, Co, Cr, Ti, Cl, and Br. The atomic ratios of 2.01–2.04 indicate more Fe deficiencies.

Nickel is the dopant; Si should be derived from the silica glass tube that is the chamber of CVT reaction; Co, Cr, and Ti are most likely to be inherited from the

impurities in nickel reagent or contamination from other sources; Br should be incorporated from the transport agent $FeBr_3$, and Cl is most likely contributed by the impurities in $FeBr_3$ starting material (99%). Bromine (below detection limit to 270 ppm) and/or silicon (1600 to 14600 ppm) have been reported as common unintentional impurities detected by PIXE (Lehner et al., 2012) and Rutherford backscattering (Tomm et al., 1995). The incorporation of Br and Cl impurities in pyrite crystal has been attributed to $(S\text{-}Cl)^{2-}$ and $(S\text{-}Br)^{2-}$ radical-ions in the crystal structure substituting for S_2^{2-} dumb-bells (Fiechter et al., 1986).

In Raman spectra of the products, the three bands are at ~344 cm^{-1}, ~380 cm^{-1}/377 cm^{-1}, ~427 cm^{-1}/430 cm^{-1} (Fig. 2), consistent with the three mostly observed bands of pyrite (anisotropic) (Mernagh and Trudu, 1993), while distinct from those of marcasite (polymorph of pyrite) with characteristic bands at 324 cm^{-1}, 387 cm^{-1}, and 532 cm^{-1} (Mernagh and Trudu, 1993). The band at ~380 cm^{-1}/377 cm^{-1} is assigned to the one totally symmetric mode A_g (in-phase stretching vibrations of S_2 dumb-bells); the bands at ~344 cm^{-1} and ~427 cm^{-1}/430 cm^{-1} correspond to the doubly degenerate mode E_g (libration of S_2 dumb-bells) and the triply degenerate mode F_g (various librational and stretching motions or their combinations of S_2 dumb-bells), respectively (Sourisseau et al., 1991).

Combining the abovementioned chemical and structural characteristics, in addition to the pale-yellow color and cubic and octahedral crystal forms, the products are FeS_2 pyrite.

The CVT reaction

The CVT reaction synthesizing pyrite with FeS and S as the starting materials and $FeBr_3$ as the transport agent in this study can be simplified into five steps. At the hot end of the silica glass tube, solid sulfur powders firstly sublimed to sulfur gases. The sulfur gas was then reacted with FeS, forming FeS_2 (Equation 1). The newly formed solid phase FeS_2 was subsequently reacted with $FeBr_3$ gas, generating transportable $FeBr_2$ and sulfur gases (Fiechter et al., 1986; forward equation of Equation 2). $FeBr_2$ and sulfur gases were then transported towards the cold end of the tube driven by the temperature and concentration gradients. At the cold end, $FeBr_2$ and sulfur gases reacted, yielding solid phase FeS_2 and $FeBr_3$ gas (Fiechter et al., 1986; backward equation of Equation 2).

$$FeS(s) + 1/2S_2(g) \rightarrow FeS_2(s) \quad (1)$$

$$FeS_2(s) + 2FeBr_3(g) \rightleftharpoons 3FeBr_2(g) + S_2(g) \quad (2)$$

For CVT reactions employing chlorine or bromine as the transport agent, the total pressure has been suggested to be approximately the dissociation pressure of pyrite (Fiechter et al., 1986). At temperatures of ~650 to ~550 °C (this study), the pressure, according to Fig. 3b in Fiechter et al. (1986), is lower than the threshold of 3 bar, below

This is the peer-reviewed, final accepted version for American Mineralogist, published by the Mineralogical Society of America.
The published version is subject to change. Cite as Authors (Year) Title. American Mineralogist, in press.
DOI: https://doi.org/10.2138/am-2023-9029. http://www.minsocam.org/

which the gas motion from hot to cold end is via diffusion rather than convection (Schmidt et al., 2013 and references therein).

For the dopant Ni, as no other phase(s) (e.g., NiS_x) other than pyrite is observed in the products at the cold end, additionally, some NiS_x phase(s) are stable under the conditions of the cold end (e.g., Waldner and Pelton, 2004; Kitakaze et al., 2011), thus it is less likely that metal nickel was reacted with sulfur gases forming NiS_x (Equation 3), and then NiS_x was reacted with $FeBr_3$ generating transportable $NiBr_2$ gases (Equation 4) at the hot end; instead, it is more likely that metal nickel was reacted directly with $FeBr_3$ forming $NiBr_2$ gases (Equation 5). Arriving at the cold end, $NiBr_2$ and $FeBr_2$ gases reacted, and nickel was deposited as metal nickel storing in the crystal structure of pyrite.

$$Ni(s) + x/2S_2(g) \rightarrow NiS_x(s) \quad (3)$$

$$NiS_x(s) + 2FeBr_3(g) \rightleftharpoons 2FeBr_2(g) + NiBr_2(g) + x/2S_2(g) \quad (4)$$

$$Ni(s) + 2FeBr_3(g) \rightleftharpoons 2FeBr_2(g) + NiBr_2(g) \quad (5)$$

Heterogeneity of Ni in CVT-synthesized pyrite

The intended doped Ni concentrations (calculated as bulk based on the amounts of FeS, S, Ni) are 3.4 wt% in PY3, 6.5 wt% in PY4, and 12.0 wt% in PY6 (the amounts of starting materials are listed in Supplementary Table 4). However, the Ni contents of the pyrite products show significant heterogeneity among and within grains (Fig. 5): 39 to 27300 ppm in PY3, 24 to 21700 ppm in PY4, and 57 to 2610 ppm in PY6. The lower maximum Ni concentration value measured in PY6 is most likely a sampling bias, with the spot analyses being unintentionally concentrated in regions/grains with low to medium Ni abundances.

Some previous studies have also measured the concentrations of dopant(s) in CVT-synthesized pyrite. Lehner et al. (2012) analyzed the bulk concentrations of trace elements in CVT-synthesized pyrite using ICPMS and IC-AES, and measured in situ the abundances of Ni and Co using SIMS and the contents of As by Rutherford backscattering; however, the intra- and inter-grain variations of the concentrations were not reported. Lehner et al. (2006) determined the concentrations of Ni, Co, and As in CVT-grown pyrite using LA-ICPMS, and the results show variations of up to 429 ppm for Ni, 2198 ppm for Co, and 680 ppm for As in pyrite crystals synthesized with the same amount of dopants.

Tomm et al. (1995) pointed out that it is necessary to adapt the growth velocity of pyrite crystals to the diffusion conditions for the dopant element. They attributed the inhomogeneous dopant distribution to the high growth rate of pyrite crystals. In the CVT-grown pyrite crystals of this study, voids are occasionally observed (Figs. 1 and 5), which can arise from high growth rate. The fast growth rate of pyrite crystals at the cold end with uncoupled $NiBr_2$ gas motion from hot end to cold end may thus be the cause of

the significant variations of Ni contents.

Homogeneity of $^{34}S/^{32}S$ in CVT-synthesized pyrite

The undoped PY5 have a mean $\delta^{34}S$ value of 17.9‰, with 2SD of 0.8‰. PY3, PY4, and PY6 have mean $\delta^{34}S$ values of 17.3 ± 0.9‰ (2SD), 17.7 ± 0.8‰, and 17.7 ± 0.6‰, respectively.

The ranges of $\delta^{34}S_{V\text{-}CDT}$ values of pyrite reference materials (Ruttan pyrite, Balmat pyrite, Sierra pyrite, Sonora pyrite, Maine pyrite, Isua278474 pyrite, Isua248474 pyrite, PPP-1 pyrite, Py-1 pyrite, Car111 pyrite, and Gabon pyrite) applied to the determination of sulfur isotopic composition in previous studies (Philippot et al., 2007; Cabral et al., 2013; Farquhar et al., 2013; Ireland et al., 2014; LaFlamme et al., 2016; Gallagher et al., 2017; Ward et al., 2017; Drake et al., 2018; Philippot et al., 2018; Teles et al., 2020; Chen and Campbell, 2021; Li et al., 2018; Li et al., 2021; Liu et al., 2021) are summarized in Table 5, and all the compiled data and the related references are presented in Supplementary Table 5. The homogeneity of the $\delta^{34}S_{V\text{-}CDT}$ of CVT-synthesized pyrite in this study (2SD = 0.6−0.9‰) is comparable to or even better than that of Balmat pyrite (2SD = 0.2−1.4‰), Maine pyrite (2SD = 0.8−1.5‰), Isua278474 pyrite (2SD = 0.5−1.0‰), Isua248474 pyrite (2SD = 0.9‰), Py-1 pyrite (2SD = 1.1‰), Car111 pyrite (2SD = 2.5‰), and Gabon pyrite (2SD = 1.1‰) (Table 5), which were used as secondary reference materials in the literature. Nevertheless, compared with the relatively homogeneous $\delta^{34}S_{V\text{-}CDT}$ of primary reference materials such as Ruttan pyrite (2SD = 0.1−0.6‰), Sierra pyrite (2SD = 0.2‰), Sonora pyrite (2SD = 0.2‰), and PPP-1 pyrite (2SD = 0.3‰), the $\delta^{34}S_{V\text{-}CDT}$ of the CVT-grown pyrite in this study are still slightly dispersed.

Possible sources of $^{34}S/^{32}S$ variation_$^{34}S/^{32}S$ heterogeneity in starting materials

The starting FeS powder is relatively homogeneous in $^{34}S/^{32}S$, with an average $\delta^{34}S$ value of 19.0‰ and 2SD of 0.3‰; by comparison, the $^{34}S/^{32}S$ of sulfur powder shows slight heterogeneity, with $\delta^{34}S$ values varying from 16.9‰ to 17.8‰ (2SD = 0.9‰) (Supplementary Table 8).

For PY3 pyrites, all sulfur is derived from S powder, thus the $^{34}S/^{32}S$ heterogeneity in the starting S powder can be inherited by the synthesized pyrite products. For PY4, PY5, and PY6 pyrites, the $\delta^{34}S$ values are determined by the molar ratio of the FeS powder-derived sulfur ($S_{FeS\ powder}$) to the S powder-derived sulfur ($S_{S\ powder}$) in pyrite products, as well as the $\delta^{34}S$ values of the starting FeS and S powders. One possibility is that the reactions strictly and simply follow Equations 1 and 2, i.e., a $S_{FeS\ powder}/S_{S\ powder}$ ratio of 1:1. In this case, the pyrite products can have $\delta^{34}S$ values of 17.9 to 18.5‰,

This is the peer-reviewed, final accepted version for American Mineralogist, published by the Mineralogical Society of America.
The published version is subject to change. Cite as Authors (Year) Title. American Mineralogist, in press.
DOI: https://doi.org/10.2138/am-2023-9029. http://www.minsocam.org/

which agree with the measured values (both bulk and in-situ) considering the associated uncertainties. However, this is not the only possibility, because after all, the actual reactions are much more complicated, e.g., in Equation 2, the backward reaction depositing pyrite at the cold end can potentially involve more sulfur gases stemming from S powder. Therefore, the $S_{FeS\ powder}/S_{S\ powder}$ ratio can be various.

For both possibilities, to increase the homogeneity of CVT-synthesized pyrite, one effective way is suppressing the heterogeneity of the starting materials. For the latter possibility, an additional potentially effective measure is using starting FeS and S powders with the same $\delta^{34}S$.

Possible sources of $^{34}S/^{32}S$ variation_kinetic fractionations during CVT reaction

The majority of the pyrite crystals show an increasing trend in $\delta^{34}S$ from one side to the other side of the grain (Supplementary Figs. 1 and 2). It is noteworthy that pyrite crystals during CVT reaction grew on the wall of silica glass tube, i.e., the crystals grew from one side to the other. Therefore, another possible source is the kinetic fractionations during the five main steps of CVT reaction: (1) sublimation of solid sulfur, (2) combination of solid FeS with sulfur gas forming solid FeS_2, (3) transformation of solid FeS_2 to $FeBr_2$ and S_2 gases, (4) transport of $FeBr_2$ and S_2 gases across the tube, and (5) deposition of $FeBr_2$ and S_2 gases to solid FeS_2.

Theoretically, according to the Arrhenius equation $k = Ae^{-Ea/RT}$ (k is reaction rate constant, A is frequency or pre-exponential factor, E_a is activation energy, R is gas constant, T is temperature), at the same temperature, light isotope ^{32}S has lower value of E_a, thus higher reaction rate constant, and reacts more rapidly than heavy isotope ^{34}S. Therefore, the chemical reactions (combination of solid phase FeS with sulfur gas, transformation of solid phase FeS_2 to $FeBr_2$ and S_2 gases, and deposition of $FeBr_2$ and S_2 gases to solid phase FeS_2) can potentially induce $^{34}S/^{32}S$ isotopic fractionation, which results in lower $\delta^{34}S$ values of earlier-deposited pyrite crystals and higher $\delta^{34}S$ of later-precipitated ones. In addition to the effects of mass difference of isotopes, the condensation site (e.g., close to the source, intermediate, and at the far cold end) of pyrite crystals is also an important factor, as specific sites correspond to different temperatures. It has been theoretically demonstrated that during condensation the saturation vapor pressure ($P_{j,sat}$) of the species containing the isotopes of interest is a significant determining factor for the net isotope fractionation (α_{cond}) (Equation 43 in Bourdon and Fitoussi, 2020), and $P_{j,sat}$ is a function of temperature (Davis and Richter, 2014). Therefore, the various condensation sites are also a source of $\delta^{34}S$ variation.

Apart from the chemical reactions of CVT, the gas motion (predominantly $FeBr_2$ and S_2 gases) from hot end to cold end, which is a process of diffusion rather than convection as discussed in Section 4.2, is also a plausible contributor to the $\delta^{34}S$ heterogeneity. As

This is the peer-reviewed, final accepted version for American Mineralogist, published by the Mineralogical Society of America.
The published version is subject to change. Cite as Authors (Year) Title. American Mineralogist, in press.
DOI: https://doi.org/10.2138/am-2023-9029. http://www.minsocam.org/

has been experimentally demonstrated recently, thermal (Soret) diffusion does induce sulfur isotope fractionation, up to 2.1‰ for $\delta^{34}S$ at a temperature gradient of ~175 °C under conditions of 1500 °C and 1.45 GPa for basaltic substrate with pyrite sulfur (Fortin et al., 2019). The magnitude of thermal diffusion-induced isotope fractionation has been quantified experimentally and theoretically, for instance,

$\Delta^{X}M = -\int_{T_0}^{T} \Delta S_T dT$ (Huang et al., 2010)

$\Delta^{X}M \approx A\ln(T/T_0)$ (Li and Liu, 2015)

where $\Delta^{X}M$ is the fractionation of $\delta^{X}M$, X is the mass of heavy isotope, T_0 is the reference temperature, T is the temperature at another position, S_T is the Soret coefficient, $\Delta S_T = (S_T)_{m^*} - (S_T)_m$, $A = -3/2\ln(m^*/m) - \ln(\sigma/\sigma^*)$, m^* and m are the heavy and light isotopes, respectively, σ is the symmetry number. It is difficult to determine the exact sulfur isotopic fractionation at a given T due to the lack of parameter values such as S_T of sulfur species S_2 under the conditions of this study. Nevertheless, the equations indicate that the degree of such fractionation is dependent on T, i.e., condensation site of pyrite crystals in the case of CVT.

Collectively, kinetic isotope fractionations stemming from the chemical reactions and thermal diffusion during CVT as well as different condensation sites potentially contributed to the $\delta^{34}S$ heterogeneity of pyrite, although at present it is difficult to quantitatively estimate the total kinetic isotopic fractionations during the CVT reaction due to the lack of pertinent determined parameters.

Possible sources of $^{34}S/^{32}S$ variation_matrix effects

In this study, the in-situ $\delta^{34}S$ values of undoped PY5 show deviations of −0.6 to 0.5‰ ($\Delta^{34}S = \delta^{34}S_{SIMS(in\text{-}situ)} - \delta^{34}S_{IRMS(bulk)}$) from the bulk $\delta^{34}S$ value (Supplementary Table 6; Fig. 6), which can be attributed to the analytical uncertainties of both in-situ and bulk $\delta^{34}S$ (2σ = 0.7 to 0.9‰, calculated following $2\sigma = [(\text{external error of in-situ } \delta^{34}S)^2 + (\text{analytical error of bulk } \delta^{34}S)^2]^{0.5}$). For Ni-doped pyrites with a range of concentrations of Ni, the magnitudes of the discrepancies between in-situ and bulk $\delta^{34}S$ values are −0.9 to 0.4‰ for PY3 (2σ = 0.7 to 0.9‰), −1.0 to 0‰ for PY4 (2σ = 0.7 to 0.9‰), and −0.9 to 0.3‰ for PY6 (2σ = 0.8 to 0.9‰). The majority of the offsets are within the associated uncertainties, with the exception of four data points displaying larger magnitudes of $\Delta^{34}S$ (−0.8‰, −0.9‰, −1.0‰, −1.0‰) than the related uncertainties (0.7‰, 0.7‰, 0.8‰, 0.7‰). Such deviations are likely to arise from matrix effects.

The matrix effects of impurities in pyrite on the determination of $^{34}S/^{32}S$ have rarely been investigated. Riciputi et al. (1998) studied the effects of instrumental parameters, including primary ion beam, secondary ion energy, and polarity on the measurements of $^{34}S/^{32}S$ using a modified Cameca 4f ion microprobe. They found that the bias for sulfur

isotope measurement is small (several per mil) compared with that for carbon and oxygen isotopes (tens of per mil) when using Cs^+ as primary ions.

Regression of all the data points for PY3, PY4, and PY6 (excluding the two with positive $\Delta^{34}S$) as well as the data point for Norilsk pentlandite (average Ni content of 38.2 wt%, Supplementary Table 7, and $\Delta^{34}S$ of −1.3‰ calibrated to Ruttan pyrite, Supplementary Table 3) yields an empirical calibration equation of $\Delta^{34}S(‰) = -0.59 \times Ni(wt\%)^{0.27}$ ($R^2 = 0.3$), where $\Delta^{34}S$ is the discrepancy between in-situ and bulk $\delta^{34}S$ values, Ni is the concentration of nickel in pyrite. Although pentlandite has a different crystal structure compared with pyrite, we still roughly view it as the high-Ni pyrite end member based on similar count rate (CPS) of secondary sulfur ions (slightly lower, Supplementary Table 3; Fig. 6). It can be predicted from the above equation that the matrix effects of nickel in pyrite are restricted within a small magnitude (around −1‰). Admittedly, the small magnitudes of $\Delta^{34}S$ corresponding to low Ni contents (<0.26 wt%) show large uncertainties, and the pertinent data points are quite scattered. Regression incorporating only data points with Ni concentration higher than 0.26 wt.% yields a line with an equation of $\Delta^{34}S$ (‰) = −0.02Ni (wt%) – 0.69 ($R^2 = 0.6$). However, the line and the curve are close, with the maximum discrepancy being approximately 0.3‰ (calculated from $-0.02Ni - 0.69 + 0.59 \times Ni^{0.27}$), therefore, we still use the equation of $\Delta^{34}S = -0.59 \times Ni^{0.27}$ for empirical calibration.

When calibrating other Fe- and S-bearing sulfides (chalcopyrite, arsenopyrite, pyrrhotite) against Ruttan pyrite, the biases ($\Delta^{34}S = \delta^{34}S_{SIMS} - \delta^{34}S_{IRMS}$) vary from sulfide to sulfide in both magnitude and sign (Supplementary Tables 9 and 10). The Norilsk pentlandite shows a bias of −1.3 ± 0.6‰ (2SD) with the same sign as that of Ni-bearing pyrite. The YJS65 arsenopyrite (Xie et al., 2019) displays a larger bias of −2.3 ± 0.8‰ (2SD), and one session even gives a bias up to −5.0‰. In contrast, the Norilsk chalcopyrite exhibits a positive bias of 0.5 ± 0.6‰ (2SD), with the bias of only one session being 2.7‰. In comparison, the bias of pyrrhotite is more intricate. In this study, Anderson pyrrhotite displays a positive bias of 0.4 ± 0.3‰ (2SD) and a negative bias of −0.7 ± 0.5‰ (2SD), YP136 pyrrhotite (Li et al., 2019) shows a positive bias of 1.6 ± 0.8‰ (2SD); in Liu et al. (2020), Anderson pyrrhotite exhibits a positive bias of 0.3 ± 0.5‰ (2SD) and a negative bias of −0.3 ± 0.4‰ (2SD). Such complex biases of pyrrhotite may be attributed to various S/Fe ratios in different pyrrhotite grains.

The respective negative and positive biases ($\Delta^{34}S$) of arsenopyrite and chalcopyrite correlate with lower and higher sulfur ion yields ($^{32}S^-$, CPS) and sulfur contents, higher and lower iron contents (Fig. 7a, c, d). However, when involving pentlandite and pyrrhotite, there are no correlations as a whole. Nevertheless, the bias shows a good correlation with the discrepancy between the sulfur ion yields of other sulfides and that of Ruttan pyrite in the same SIMS analytical session (Fig. 7b). The kinetic mechanism of Eiler et al. (1997) can be used to explain the bias of chalcopyrite ($CuFeS_2$), as copper has

a higher atomic mass of 63.5 amu than iron (55.8 amu). During sputtering, chalcopyrite transfers kinetic energy more efficiently to ^{34}S than to ^{32}S compared with pyrite (FeS_2), thus giving rise to larger $\delta^{34}S$ values. However, this mechanism cannot account for the biases of arsenopyrite (FeAsS) and pentlandite [$(Ni_xFe_y)_9S_8$].

IMPLICATIONS

Based on the relatively uniform distribution of $^{34}S/^{32}S$, the CVT-synthesized pyrite has the potential to be applied as reference material for the *in-situ* measurement of sulfur isotopes using techniques such as SIMS and LA-ICPMS. The inevitable impurities (e.g., Br, Cl, Si) can potentially have effects on the sputtering of the target mineral surface by primary ions of SIMS, thus the secondary ion yields and instrumental mass fractionation (i.e., mineral chemistry- and/or structure-induced matrix effects, Ireland, 2004 and references therein). Ruttan pyrite and Balmat pyrite contain similar low amounts (up to several hundred ppm) of Si and Cl to CVT-grown pyrite as well as other trace elements (Table 2), however, such matrix effects have not been observed. Previous reported matrix effects caused by chemical impurities are of major elements (e.g., Rollion-Bard and Marin-Carbonne, 2011; Vho et al., 2020). As such, given the low concentrations of these impurities in CVT-synthesized pyrite, such effects can be negligible. One exception is that high concentrations of Br (up to 31200 ppm) are observed in a few grains in this study. Further investigations are needed to assess whether such high contents of Br give rise to observable matrix effects in sulfur isotope measurements by SIMS.

CONCLUDING REMARKS

This study synthesized pyrite crystals via Chemical Vapor Transport (CVT) reaction. The pyrites contain traces of impurities such as Si, Br, Cl, Co, Cr, Se, Ti, which can be derived from the starting materials and silica glass reaction tube. The nickel concentrations of nickel-doped pyrites are heterogeneous, at both inter- and intra-grain scales, which can be attributed to the high growth rate of pyrite crystals with uncoupled motion rate of $NiBr_2$ gas. In contrast, the sulfur isotopic compositions ($\delta^{34}S$) of these pyrites are relatively homogeneous despite slightly dispersed compared with currently used primary reference materials (e.g., Ruttan pyrite). The variations in $\delta^{34}S$ can arise from the slight heterogeneity of $\delta^{34}S$ in starting materials, the kinetic isotopic fractionations during the chemical and physical processes of CVT reaction and different condensation sites in tubes, as well as the minor matrix effects of nickel for SIMS analysis. An empirical equation was obtained for the calibration of the matrix effects of nickel in pyrite: $\Delta^{34}S$ (‰) = $-0.59 \times Ni(wt\%)^{0.27}$. Based on the homogeneity of $^{34}S/^{32}S$, CVT-grown pyrite has the potential to be used as reference material for *in-situ*

measurement of sulfur isotopes in pyrite using techniques such as SIMS and LA-ICPMS.

ACKNOWLEDGEMENTS

Dr. Jeff Chen, Dr. Monika Misztela, and Prof. Ian Williams assisted with EPMA, LA-ICP-MS, and SHRIMP analyses, respectively. The authors acknowledge the facilities and the scientific and technical assistance of Microscopy Australia at CAM, ANU. We thank Dr. Faqiao Li for the assistance in the analysis of bulk $^{34}S/^{32}S$ of starting materials. We also thank the Editor for handling this manuscript and the anonymous reviewers for their constructive comments and suggestions.

FUNDING

This work was supported by the National Natural Science Foundation of China (No. 42003002) to Li Liu and the Strategic Priority Research Program of Chinese Academy of Sciences (No. XDB42000000) to Xing Ding.

REFERENCES CITED

Bourdon, B., and Fitoussi, C., 2020. Isotope Fractionation during Condensation and Evaporation during Planet Formation Processes. ACS Earth Space Chemistry 4, 1408–1423.

Cabral, R.A., Jackson, M.G., Rose-Koga, E.F., Koga, K.T., Whitehouse, M.J., Antonelli, M.A., Farquhar, J., Day, J.M.D., and Hauri, E.H. (2013) Anomalous sulphur isotopes in plume lavas reveal deep mantle storage of Archaean crust. Nature, 496, 490–493.

Chen, L., Li, X.H., Li, J.W., Hofstra, A.H., Liu, Y., and Koening, A.E. (2015) Extreme variation of sulfur isotopic compositions in pyrite from the Qiuling sediment-hosted gold deposit, West Qinling orogen, central China: an in situ SIMS study with implications for the source of sulfur. Mineralium Deposita, 50, 643–656.

Chen, M., and Campbell, I.H. (2021) Kinetic factors control trace element and isotope zoning in Archean pyrite corona nodules. Geochimica et Cosmochimica Acta, 315, 230–250.

Clark, L.A. (1960) THE Fe-As-S SYSTEM: PHASE RELATIONS AND APPLICATIONS. Economic Geology, 55, 1345–1381.

Crowe, D.E. and Vaughan, R.G. (1996) Characterization and use of isotopically homogeneous standards for in situ laser microprobe analysis of $^{34}S/^{32}S$ ratios. American Mineralogist, 81, 187–193.

Davis, A.M., and Richter, F.M., 2014. Condensation and Evaporation of Solar System Materials. In: Holland, H.D., Turekian, K.K. (Eds.), Treatise on Geochemistry,

Second Edition, Elsevier, Volume 1, pp 335–360.

Diener, A., and Köppe, R. (2012) Synthesis of selenium doted pyrite single crystals prepared by chemical vapor transport. Journal of Crystal Growth, 349, 55–60.

Ding, T., Valkiers, S., Kipphardt, H., De Bièvre, P., Taylor, P.D.P., Gonfiantini, R., and Krouse, R. (2001) Calibrated sulfur isotope abundance ratios of three IAEA sulfur isotope reference materials and V-CDT with a reassessment of the atomic weight of sulfur. Geochimica et Cosmochimica Acta, 65, 2433–2437.

Drake, H., Whitehouse, M.J., Heim, C., Reiners, P.W., Tillberg, M., Hogmalm, K.J., Dopson, M., Broman, C., and Åström, M.E. (2018) Unprecedented 34S-enrichment of pyrite formed following microbial sulfate reduction in fractured crystalline rocks. Geobiology, 16, 556–574.

Eggins, S.M., Grün, R., McCulloch, M.T., Pike, A.W.G., Chappell, J., Kinsley, L., Mortimer, G., Shelley, M., Murray-Wallace, C.V., Spötle, C., and Taylor, L. (2005) In situ U-series dating by laser- ablation multi-collector ICPMS: new prospects for Quaternary geochronology. Quaternary Science Reviews, 24, 2523–2538.

Eiler, J.M., Graham, C., and Valley, J.W. (1997) SIMS analysis of oxygen isotopes: matrix effects in complex minerals and glasses. Chemical Geology, 138, 221–244.

Farquhar, J., Cliff, J., Zerkle, A.L., Kamyshny, A., Poulton, S.W., Claire, M., Adams, D., and Harms, B. (2013) Pathways for Neoarchean pyrite formation constrained by mass-independent sulfur isotopes. PNAS, 110, 17638–17643.

Feng, Y., Zhang, W., Hu, Z., Luo, T., Li, M., Liu, Y., Liu, H., and Li, Q. (2022) A new synthesis scheme of pyrite and chalcopyrite reference materials for in situ iron and sulfur isotope analysis using LA-MC-ICP-MS. Journal of Analytical Atomic Spectrometry, doi: 10.1039/D1JA00392E.

Fiechter, S., Mai, J., and Ennaoui, A. (1986) CHEMICAL VAPOUR TRANSPORT OF PYRITE (FeS_2) WITH HALOGEN (Cl, Br, I). Journal of Crystal Growth, 78, 438–444.

Fortin, M.A., Watson, E.B., Stern, R.A., and Ono, S., 2019. Experimental characterization of diffusive and Soret isotopic fractionation of sulfur in a reduced, anhydrous basaltic melt. Chemical Geology 510, 10–17.

Gallagher, M., Whitehouse, M.J., and Kamber, B.S. (2017) The Neoarchaean surficial sulphur cycle: An alternative hypothesis based on analogies with 20th-century atmospheric lead. Geobiology, 15, 385–400.

Gu, W., Cheng, P., and Tang, M. (2018) Compilation and evaluation of gas phase diffusion coefficients of halogenated organic compounds. Royal Society Open Science, 5, 171936.

Hellstrom, J., Paton, C., Woodhead, J., and Hergt, J. (2008) Iolite: Software for spatially resolved LA-(QUAD and MC) ICPMS analysis. In P. Sylvester, Ed., Laser Ablation ICP–MS in the Earth Sciences: Current Practices and Outstanding Issues pp. 343–

348. Mineralogical Association of Canada Short Course Series.

Ireland, T.R. (2004) SIMS Measurement of Stable Isotopes. In P.A. de Groot, Ed., Handbook of Stable Isotope Analytical Techniques pp. 652–691. Elsevier.

Ireland, T.R., Schram, N., Holden, P., Lanc, P., Ávila, J., Armstrong, R., Amelin, Y., Latimore, A., Corrigan, D., Clement, S., Foster, J.J., and Compston, W. (2014) Charge-mode electrometer measurements of S-isotopic compositions on SHRIMP-SI. International Journal of Mass Spectrometry, 359, 26–37.

Jochum, K.P., Weis, U., Stoll, B., Kuzmin, D., Yang, Q., Raczek, I., Jacob, D.E., Stracke, A., Birbaum, K., Frick, D.A., Günther, D., and Enzweiler, J. (2011) Determination of reference values for NIST SRM 610–617 glasses following ISO guidelines. Geostandards and Geoanalytical Research, 35, 397–429.

Jochum, K.P., Willbold, M., Raczek, I., Stoll, B., and Herwig, K. (2005) Chemical Characterisation of the USGS Reference Glasses GSA-1G, GSC-1G, GSD-1G, GSE-1G, BCR-2G, BHVO-2G and BIR-1G Using EPMA, ID-TIMS, ID-ICP-MS and LA-ICP-MS. Geostandards and Geoanalytical Research, 29, 285–302.

Kendrick, M.A. (2012) High precision Cl, Br and I determinations in mineral standards using the noble gas method. Chemical Geology, 292, 116–126.

Kitakaze, A., Sugaki, A., Itoh, H., and Komatsu, R. (2011) A revision of phase relations in the system Fe-Ni-S from 650° to 450°C. The Canadian Mineralogist 49, 1687–1710.

Kozdon, R., Kita, N.T., Huberty, J.M., Fournelle, J.H., Johnston, C.A., and Valley, J.W. (2010) In situ sulfur isotope analysis of sulfide minerals by SIMS: Precision and accuracy, with application to thermometry of ~3.5 Ga Pilbara cherts. Chemical Geology, 275, 243–253.

LaFlamme, C., Martin, L., Jeon, H., Reddy, S.M., Selvaraja, V., Caruso, S., Bui, T.H., Roberts, M.P., Voute, F., Hagemann, S., Wacey, D., Littman, S., Wing, B., Fiorentini, M., and Kilburn, M.R. (2016) In situ multiple sulfur isotope analysis by SIMS of pyrite, chalcopyrite, pyrrhotite, and pentlandite to refine magmatic ore genetic models. Chemical Geology, 444, 1–15.

Lehner, S.W., Savage, K.S., and Ayers, J.C. (2006) Vapor growth and characterization of pyrite (FeS_2) doped with Co, Ni, and As: Variations in semiconducting properties. Journal of Crystal Growth, 286, 306–317.

Lehner, S.W., Newman, N., van Schilfgaarde, M., Bandyopadhyay, S., Savage, K., and Buseck, P.R. (2012) Defect energy levels and electronic behavior of Ni-, Co-, and As-doped synthetic pyrite (FeS_2). Journal of Applied Physics, 111, 083717.

Li, R., Chen, H., Xia, X., Yang, Q., Li, L., Xu, J., Huang, C., and Danyushevsky, L.V. (2017) Ore fluid evolution in the giant Marcona Fe-(Cu) deposit, Perú: Evidence from in-situ sulfur isotope and trace element geochemistry of sulfides. Ore Geology Reviews, 86, 624–638.

739 Li, R., Xia, X., Yang, S., Chen, H., and Yang, Q. (2019) Off-Mount Calibration and One
740 New Potential Pyrrhotite Reference Material for Sulfur Isotope Measurement by
741 Secondary Ion Mass Spectrometry. Geostandards and Geoanalytical Research, 43,
742 177–187.
743 Li, R., Chen, H., Wu, N., Wang, X., and Xia, X. (2021) Multiple sulfur isotope in
744 post-Archean deposits as a potential tracer for fluid mixing processes: An example
745 from an iron oxide-copper-gold (IOCG) deposit in southern Peru. Chemical Geology,
746 575, 120230.
747 Li, R., Xia, X., Yang, S., Chen, H., and Yang, Q. (2018) Off-Mount Calibration and One
748 New Potential Pyrrhotite Reference Material for Sulfur Isotope Measurement by
749 Secondary Ion Mass Spectrometry. Geostandards and Geoanalytical Research, 43,
750 177–187.
751 Li, X., and Liu, Y., 2015. A theoretical model of isotopic fractionation by thermal
752 diffusion and its implementation on silicate melts. Geochimica et Cosmochimica
753 Acta 154, 18–27.
754 Liu, L., Ireland, T.R., Holden, P., Ávila, J., Vasconcelos, P., and Mavrogenes, J. (2021)
755 Sources of auriferous fluids associated with a Neoarchean BIF-hosted orogenic gold
756 deposit revealed by the multiple sulfur isotopic compositions of zoned pyrites.
757 Contributions to Mineralogy and Petrology, 176:29.
758 Liu, L., Mavrogenes, J., Holden, P., and Ireland, T. (2020) Quadruple sulfur isotopic
759 fractionation during pyrite desulfidation to pyrrhotite. Geochimica et Cosmochimica
760 Acta, 273, 354–366.
761 Marks, M.A.W., Kendrick, M.A., Eby, G.N., Zack, T., and Wenzel, T. (2016) The F, Cl, Br,
762 I Contents of Reference Glasses BHVO-2G, BIR-1G, BCR-2G, GSD-1G, GSE-1G,
763 NIST SRM 610 and NIST SRM 612. Geostandards and Geoanalytical Research, 41,
764 107–122.
765 Mernagh, T.P., and Trudu, A.G. (1993) A laser Raman microprobe study of some
766 geologically important sulphide minerals. Chemical Geology, 103, 113–127.
767 Muller, É., Philippot, P., Rollion-Bard, C., Cartigny, P., Assayag, N., Marin-Carbonne, J.,
768 Mohan, M.R., and Sarma, D.S. (2017) Primary sulfur isotope signatures preserved in
769 high-grade Archean barite deposits of the Sargur Group, Dharwar Craton, India.
770 Precambrian Research, 295, 38–47.
771 Paton, C., Hellstrom, J., Paul, B., Woodhead, J., and Hergt, J. (2011) Iolite: Freeware for
772 the visualisation and processing of mass spectrometric data. Journal of Analytical
773 Atomic Spectrometry, 26, 2508–2518.
774 Paton, C., Woodhead, J.D., Hellstrom, J.C., Hergt, J.M., Greig, A., and Maas, R. (2010)
775 Improved laser ablation U-Pb zircon geochronology through robust downhole
776 fractionation correction. Geochemistry, Geophysics and Geosystem, 11, Q0AA06, 1–
777 36.

778 Philippot, P., Van Zilen, M., Lepot, K., Thomazo, C., Farquhar, J., and Van Kranendonk,
779 M.J. (2007) Early Archaean Microorganisms Preferred Elemental Sulfur, Not Sulfate.
780 Science, 317, 1534–1537.
781 Philippot, P., Ávila, J.N., Killingsworth, B.A., Tessalina, S., Baton, F., Caquineau, T.,
782 Muller, E., Pecoits, E., Cartigny, P., Lalonde, S.V., Ireland, T.R., Thomazo, C., van
783 Kranendonk, M.J., and Busigny, V. (2018) Globally asynchronous sulphur isotope
784 signals require re-definition of the Great Oxidation Event. Nature Communications,
785 9: 2245, 1–10.
786 Riciputi, L.R., Paterson, B.A., and Ripperdan, R.L. (1998) Measurement of light stable
787 isotope ratios by SIMS: Matrix effects for oxygen, carbon, and sulfur isotopes in
788 minerals. International Journal of Mass Spectrometry, 178, 81–112.
789 Rickard, D. (2012) Sulfidic sediments and sedimentary rocks. In A.J. Van Loo, Ed.,
790 Developments in Sedimentology pp. 1–801. Elsevier.
791 Rollion-Bard, C., and Marin-Carbonne, J. (2011) Determination of SIMS matrix effects on
792 oxygen isotopic compositions in carbonates. Journal of Analytical Atomic
793 Spectrometry, 26, 1285–1289.
794 Schmidt, P., Binnewies, M., Glaum, R., and Schmidt, M. (2013) Chemical Vapor
795 Transport Reactions–Methods, Materials, Modeling. In S.O. Ferreira, Ed., Advanced
796 Topics on Crystal Growth https://doi.org/10.5772/55547. IntechOpen.
797 Sourisseau, C., Cavagnat, R., and Fouassier, M. (1974) The vibrational properties and
798 valence force fields of FeS_2, RuS_2 pyrites and FeS_2 marcasite. Journal of Physics and
799 Chemistry of Solids, 52, 537–544.
800 Steadman, J.A., Large, R.R., Blamey, N.J., Mukherjee, I., Corkrey, R., Danyushevsky,
801 L.V., Maslennikov, V., Hollings, P., Garven, G., Brand, U., and Lécuyer, C. (2020)
802 Evidence for elevated and variable atmospheric oxygen in the Precambrian.
803 Precambrian Research, 343, 105722.
804 Teles, G.S., Chemale Jr., F., Ávila, J.N., Ireland, T.R., Dias, A.N.C., Cruz, D.C.F., and
805 Constantino, C.J.L. (2020) Textural and geochemical investigation of pyrite in
806 Jacobina Basin, São Francisco Craton, Brazil: Implications for paleoenvironmental
807 conditions and formation of pre-GOE metaconglomerate-hosted Au-(U) deposits.
808 Geochimica et Cosmochimica Acta, 273, 331–353.
809 Tomm, Y., Schieck, R., Ellmer, K., and Fiechter, S. (1995) Growth mechanism and
810 electronic properties of doped pyrite (FeS_2) crystals. Journal of Crystal Growth, 146,
811 271–276.
812 Vho, A., Rubatto, D., Putlitz, B., and Bouvier, A.S. (2020) New Reference Materials and
813 Assessment of Matrix Effects for SIMS Measurements of Oxygen Isotopes in Garnet.
814 Geostandards and Geoanalytical Research, 44, 459–471.
815 Voigt, B., Moore, W., Maiti, M., Walter, J., Das, B., Manno, M., Leighton, C., and Aydil,
816 E.S. (2020) Observation of an Internal p-n Junction in Pyrite FeS_2 Single Crystals:

817 Potential Origin of the Low Open Circuit Voltage in Pyrite Solar Cells. ACS Materials
818 Letters, 2 (7), 861–868.
819 Waldner, P., and Pelton, A.D. (2004) Critical Thermodynamic Assessment and Modeling
820 of the Fe-Ni-S System. Metallurgical and Materials Transactions B, 35B, 897–907.
821 Walter, J., Zhang, X., Voigt, B., Hool, R., Manno, M., Mork, F., Aydil, E.S., and Leighton,
822 C. (2017) Surface conduction in n-type pyrite FeS_2 single crystals. Physical Review
823 Materials, 1, 065403.
824 Ward, J., Mavrogenes, J., Murray, A., and Holden, P. (2017) Trace element and sulfur
825 isotopic evidence for redox changes during formation of the Wallaby Gold Deposit,
826 Western Australia. Ore Geology Reviews, 82, 31–48.
827 Xian, H., Zhu, J., Liang, X., and He, H. (2016) Morphology controllable syntheses of
828 micro- and nano-iron pyrite mono- and poly-crystals: a review. RSC Advances, 6,
829 31988.
830 Xie, G., Mao, J., Li, W., Fu, B., and Zhang, Z. (2019) Granite-related Yangjiashan tungsten
831 deposit, southern China. Mineralium Deposita, 54, 67–80.

List of figure captions

Fig. 1. Photographs (a–d) and BSE images (e–h) of the crystals synthesized by CVT method in this study. Note that Ni-doped PY3, PY4, and PY6 are larger in size than undoped PY5. The white bar in (a) to (d) is for 2 mm. The gradual change in brightness horizontally in (e) to (h) is due to SEM instrumental problems rather than the crystals per se.

Fig. 2. Raman spectra of typical crystals PY3, PY4, PY5, and PY6. Note that the spectra of wavenumber higher than 1000 cm^{-1} are not plotted because they are featureless.

Fig. 3. Plot of nickel contents derived from EPMA and LA-ICPMS. The error bar is the value of 2SE.

Fig. 4. $\delta^{34}S$ variations of PY3, PY4, PY5, and PY6, along with the corresponding bulk $\delta^{34}S$ values obtained by IRMS (grey line). The error bar is external error ($\pm 2\sigma$). The thickness of the grey line is the value of 2SE, which takes the variation of bulk $\delta^{34}S$ and the uncertainty of IRMS measurement into account.

Fig. 5. BSE images of typical PY3, PY4, PY5, and PY6 CVT-synthesized pyrite grains with nickel concentrations and $\delta^{34}S$ values. Note the heterogeneity of Ni abundances (yellow, ppm) and the homogeneity of $\delta^{34}S$ (white, ‰) among polygrains and within monograins. Spot size is much smaller than the circles. Again the gradual change in brightness horizontally in these BSE images is due to SEM instrumental problems rather than the crystals per se.

Fig. 6. Plot of nickel contents obtained by LA-ICPMS (transformed to wt.%) vs. the deviation magnitudes of in-situ $\delta^{34}S$ values from bulk $\delta^{34}S$ values ($\Delta^{34}S = \delta^{34}S_{in\text{-}situ} - \delta^{34}S_{bulk}$). For curve fitting, the data points of PY5 and those with positive $\Delta^{34}S$ values are excluded; the data point (38.2 wt.%, −1.3‰, average values) for the Norilsk pentlandite is incorporated. The average error of $\Delta^{34}S$ (1σ) is 0.4‰, which includes the external error of in-situ $\delta^{34}S$ and the error of bulk $\delta^{34}S$; the average error of Ni content (1σ = 0.0038 wt.%) of pyrite is too small to be displayed; the average error (1σ) of Ni content of Norilsk pentlandite is displayed.

Fig. 7. (a) Plot of secondary sulfur ion ($^{32}S^-$) yield (CPS, counts per second) vs. the magnitudes of $\delta^{34}S$ bias ($\Delta^{34}S = \delta^{34}S_{in\text{-}situ} - \delta^{34}S_{bulk}$), $\delta^{34}S_{in\text{-}situ}$ was obtained by calibration against Ruttan pyrite. (b) Plot of discrepancy of secondary sulfur ion yield between other sulfides and Ruttan pyrite in the same session [$(CPS_{32S-})_{other\ sulfide} - (CPS_{32S-})_{Ruttan\ Pyrite}$)]

vs. the magnitudes of $\Delta^{34}S$. Anderson pyrrhotite_BF are from this study, and Anderson pyrrhotite_LL are from Liu et al. (2020). All the related data are listed in Supplementary Tables 9 and 10. (c) Plot of S content in sulfides vs. $\Delta^{34}S$. (d) Plot of Fe content in sulfides vs. $\Delta^{34}S$. The sulfur and iron contents in Anderson Pyrrhotite are cited from Kozdon et al. (2010), those in YP136 Pyrrhotite are cited from Li et al. (2019), those of YJS65 Arsenopyrite and Norilsk Chalcopyrite are calculated from their ideal formulae. The uncertainty of $\Delta^{34}S$ incorporated that of both $\delta^{34}S_{in\text{-}situ}$ and $\delta^{34}S_{bulk}$.

Supplementary Fig. 1. The map of Mount Z7100 with PY3 and PY4 pyrite grains. Also shown are the $\delta^{34}S$ values (‰, green numbers) and Ni contents (ppm, blue numbers). The white ellipse only illustrates the location of each spot analysis, and the size is not the actual spot size. The yellow dashed lines with arrow are the direction with an increasing trend of $\delta^{34}S$, which can be pyrite crystal growth direction.

Supplementary Fig. 2. The map of Mount Z7102 with PY5 and PY6 pyrite grains. Also shown are the $\delta^{34}S$ values (‰, green numbers) and Ni contents (ppm, blue numbers). The white ellipse only illustrates the location of each spot analysis, and the size is not the actual spot size. The yellow dashed lines with arrow are the direction with an increasing trend of $\delta^{34}S$, which can be pyrite crystal growth direction.

This is the peer-reviewed, final accepted version for American Mineralogist, published by the Mineralogical Society of America.
The published version is subject to change. Cite as Authors (Year) Title. American Mineralogist, in press.
DOI: https://doi.org/10.2138/am-2023-9029. http://www.minsocam.org/

Table 1. EPMA-determined major element contents of synthetic products, Ruttan pyrite and Balmat pyrite

	PY3	**PY4**	**PY5**	**PY6**	**Ruttan Pyrite**	**Balmat Pyrite**
S ± 2SD (wt.%)	54.20 ± 0.32	54.18 ± 0.23	54.06 ± 0.37	54.05 ± 0.38	54.08 ± 0.31	54.13 ± 0.15
Fe ± 2SD (wt.%)	46.37 ± 1.32	46.71 ± 0.91	46.86 ± 0.28	46.63 ± 0.42	46.81 ± 0.32	46.83 ± 0.35
Ni ± 2SD (wt.%)	0.44 ± 1.18	0.18 ± 0.89	0.00 ± 0.01	0.12 ± 0.17	0.00 ± 0.00	0.00 ± 0.00
$(S/Fe)_{weight}$ ± 2SD	1.17 ± 0.03	1.16 ± 0.02	1.15 ± 0.01	1.16 ± 0.01	1.16 ± 0.01	1.16 ± 0.01
$(S/Fe)_{atom}$ ± 2SD	2.04 ± 0.06	2.02 ± 0.04	2.01 ± 0.02	2.02 ± 0.02	2.01 ± 0.02	2.01 ± 0.02

This is the peer-reviewed, final accepted version for American Mineralogist, published by the Mineralogical Society of America.
The published version is subject to change. Cite as Authors (Year) Title. American Mineralogist, in press.
DOI: https://doi.org/10.2138/am-2023-9029. http://www.minsocam.org/

Table 2. LA-ICPMS-determined trace element concentrations in synthetic products, Ruttan pyrite and Balmat pyrite

Trace element	PY3	PY4	PY5	PY6	Ruttan pyrite	Balmat pyrite
Ni (ppm)	39–27300	24–21700	BDL–2	57–2610	0–1	8–13
Si (ppm)	268–446	249–520	282–487	281–399	312–472	302–404
Br (ppm)	BDL–31200	BDL–910	BDL–880	BDL–1860	BDL[b]	BDL[a]
Se (ppm)	BDL	BDL	BDL	BDL	9–16	BDL
Co (ppm)	0–56	BDL–59	0–9	0–6	53–70	2–14
Cr (ppm)	1–86	BDL–1	BDL–2	BDL[c]	BDL	BDL
Ti (ppm)	9–12	9–12	8–11	9–12	10–11	10–11
Cl (ppm)	24–53	BDL–54	BDL–64	23–45	25–46	30–43

Notes: a. BDL: Below detection limit. b. One analysis of Ruttan pyrite shows Br content of 29 ppm. c. One analysis is 0.46 ppm.

This is the peer-reviewed, final accepted version for American Mineralogist, published by the Mineralogical Society of America.
The published version is subject to change. Cite as Authors (Year) Title. American Mineralogist, in press.
DOI: https://doi.org/10.2138/am-2023-9029. http://www.minsocam.org/

Table 3. Sulfur isotope data for synthetic products, Ruttan pyrite, and Balmat pyrite determined by SHRIMP-SI

	Reference materials		**CVT-synthesized pyrites**			
	Primary	**Secondary**	**PY3**	**PY4**	**PY5**	**PY6**
	Ruttan pyrite	**Balmat pyrite**				
N	45	10	26	26	32	22
δ^{34}S (‰)	1.2	15.4	17.3	17.7	17.9	17.7
±2SD (‰)	0.6	0.7	0.9	0.8	0.8	0.6

This is the peer-reviewed, final accepted version for American Mineralogist, published by the Mineralogical Society of America.
The published version is subject to change. Cite as Authors (Year) Title. American Mineralogist, in press.
DOI: https://doi.org/10.2138/am-2023-9029. http://www.minsocam.org/

Table 4. Bulk sulfur isotopic compositions of synthetic products measured by IRMS

	PY3			PY4			PY5			PY6	
	PY3-1	**PY3-2**	**PY3-3**	**PY4-1**	**PY4-2**	**PY4-3**	**PY5-1**	**PY5-2**	**PY5-3**	**PY6-1**	**PY6-2**
δ^{34}S (‰)	17.9	17.8	17.8	18.4	18.8	17.9	18.1	18.3	18.1	18.1	18.2
Mean (‰)		17.8			18.3			18.2		18.1	
±2SD (‰)		0.2			0.9			0.3		0.1	
±2SE (‰)		0.1			0.5			0.2		0.1	

This is the peer-reviewed, final accepted version for American Mineralogist, published by the Mineralogical Society of America.
The published version is subject to change. Cite as Authors (Year) Title. American Mineralogist, in press.
DOI: https://doi.org/10.2138/am-2023-9029. http://www.minsocam.org/

Table 5. Summarization of the $\delta^{34}S_{V\text{-}CDT}$ ranges of pyrite reference materials in the literature

Pyrite	Lab	Max. (‰)	Min. (‰)	Avg. (‰)	2SD (‰)	N	Reference
Ruttan pyrite	RSES,ANU	1.5	0.6	1.2	0.5	11	Ireland et al., 2014
		1.7	0.7	1.2	0.6	16	Ward et al., 2017
		2.2	0.7	1.2	0.3	210	Philippot et al., 2018
		1.8	0.8	1.2	0.4	99	Teles et al., 2020
		2.0	0.6	1.2	0.6	63	Chen and Campbell, 2021
		1.6	0.8	1.2	0.3	124	Liu et al., 2021
	NordSIMS	1.9	0.8	1.4	0.6	23	Cabral et al., 2013
		2.0	0.7	1.4	0.3	349	Drake et al., 2018
		1.6	1.2	1.4	0.1	30	Gallagher et al., 2017
Balmat pyrite	RSES,ANU	16.2	15.8	16.0	0.4	7	Ireland et al., 2014
		15.8	13.9	15.0	0.9	115	Philippot et al., 2018
		16.0	14.5	15.2	0.6	50	Teles et al., 2020
		16.3	14.7	15.5	0.9	21	Chen and Campbell, 2021
		15.8	13.9	14.9	0.9	63	Liu et al., 2021
	NordSIMS	16.9	14.0	16.1	1.4	15	Cabral et al., 2013
		16.4	14.0	15.9	1.3	15	Gallagher et al., 2017
	GIGCAS	16.4	15.3	16.0	0.4	90	Li et al., 2018
		16.3	14.7	15.6	1.0	23	Li et al., 2021
	CMCA,UWA	16.4	15.9	16.2	0.2	40	LaFlamme et al., 2016
Sierra pyrite	CMCA,UWA	2.7	1.5	2.2	0.2	1417	LaFlamme et al., 2016
Sonora pyrite	CMCA,UWA	2.1	1.3	1.6	0.2	247	Farquhar et al., 2013
Maine pyrite	CRPG,Nancy	−18.5	−20.3	−19.3	0.8	24	Philippot et al., 2007
	RSES,ANU	−18.1	−22.2	−20.4	1.5	136	Philippot et al., 2018
Isua^{278474} pyrite	NordSIMS	3.3	1.3	2.6	1.0	14	Cabral et al., 2013
		2.7	2.2	2.4	0.5	7	Gallagher et al., 2017
Isua^{248474} pyrite	CMCA,UWA	3.2	1.2	2.6	0.9	216	LaFlamme et al., 2016
PPP-1 pyrite	GIGCAS	6.3	5.5	5.9	0.3	180	Li et al., 2018
		6.0	5.0	5.3	0.3	95	Li et al., 2021

This is the peer-reviewed, final accepted version for American Mineralogist, published by the Mineralogical Society of America.
The published version is subject to change. Cite as Authors (Year) Title. American Mineralogist, in press.
DOI: https://doi.org/10.2138/am-2023-9029. http://www.minsocam.org/

Pyrite	Lab	Max. (‰)	Min. (‰)	Avg. (‰)	2SD (‰)	N	Reference
Py-1 pyrite	GIGCAS	0.5	−0.9	−0.1	1.1	17	Li et al., 2021
Car111 pyrite	CRPG,Nancy	18.8	15.4	16.8	2.5	9	Philippot et al., 2007
Gabon pyrite	NordSIMS	−25.5	−27.4	−26.4	1.1	11	Cabral et al., 2013

Notes: The detailed compiled data and related references are listed in Supplementary Table 5. RSES, ANU: Research School of Earth Sciences, The Australian National University; NordSIMS: Swedish Museum of Natural History; GIGCAS: Guangzhou Institute of Geochemistry, Chinese Academy of Sciences; CMCA, UWA: Centre for Microscopy, Characterisation and Analysis, University of Western Australia; CRPG, Nancy: Centre de Recherches Pétrographiques et Géochimiques, Nancy.

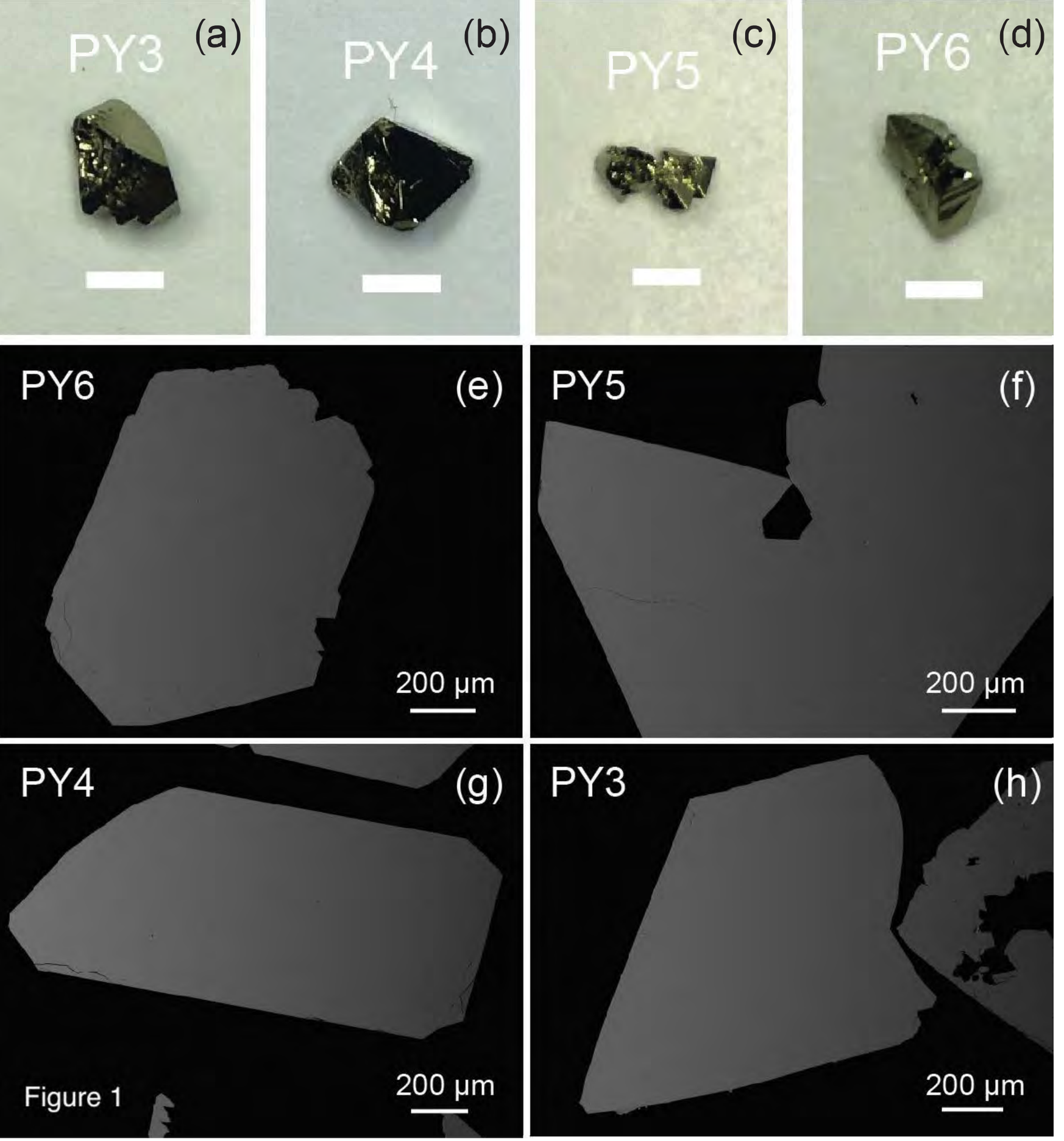
PY3
(a)
PY4
(b)
PY5
(c)
PY6
(d)
PY6
(e)
200 µm
PY5
(f)
200 µm
PY4
(g)
200 µm
PY3
(h)
200 µm

Figure 1

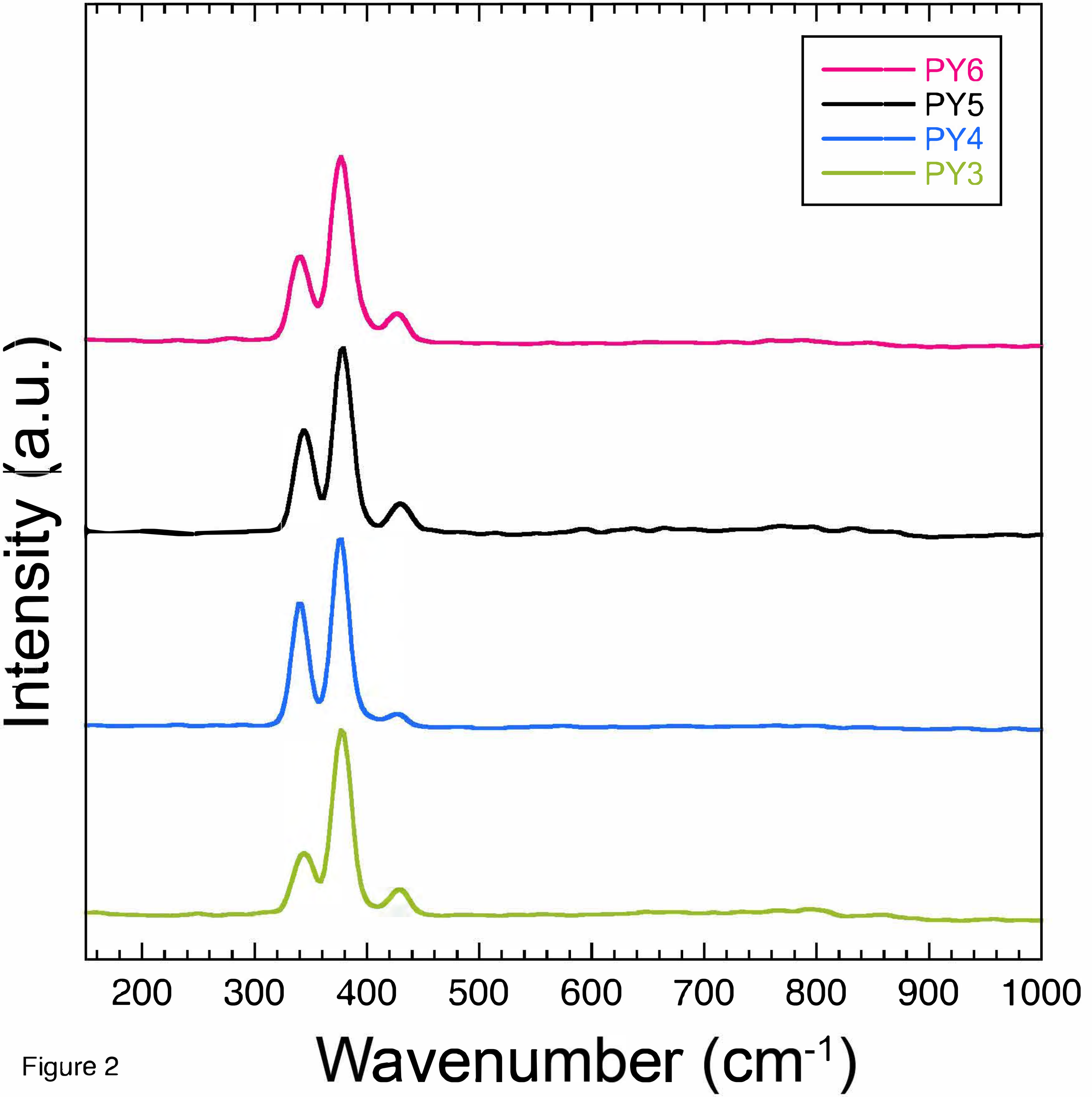
PY6
PY5
PY4
PY3
Intensity (a.u.)
200
300
400
500
600
700
800
900
1000
Wavenumber (cm-1)

Figure 2

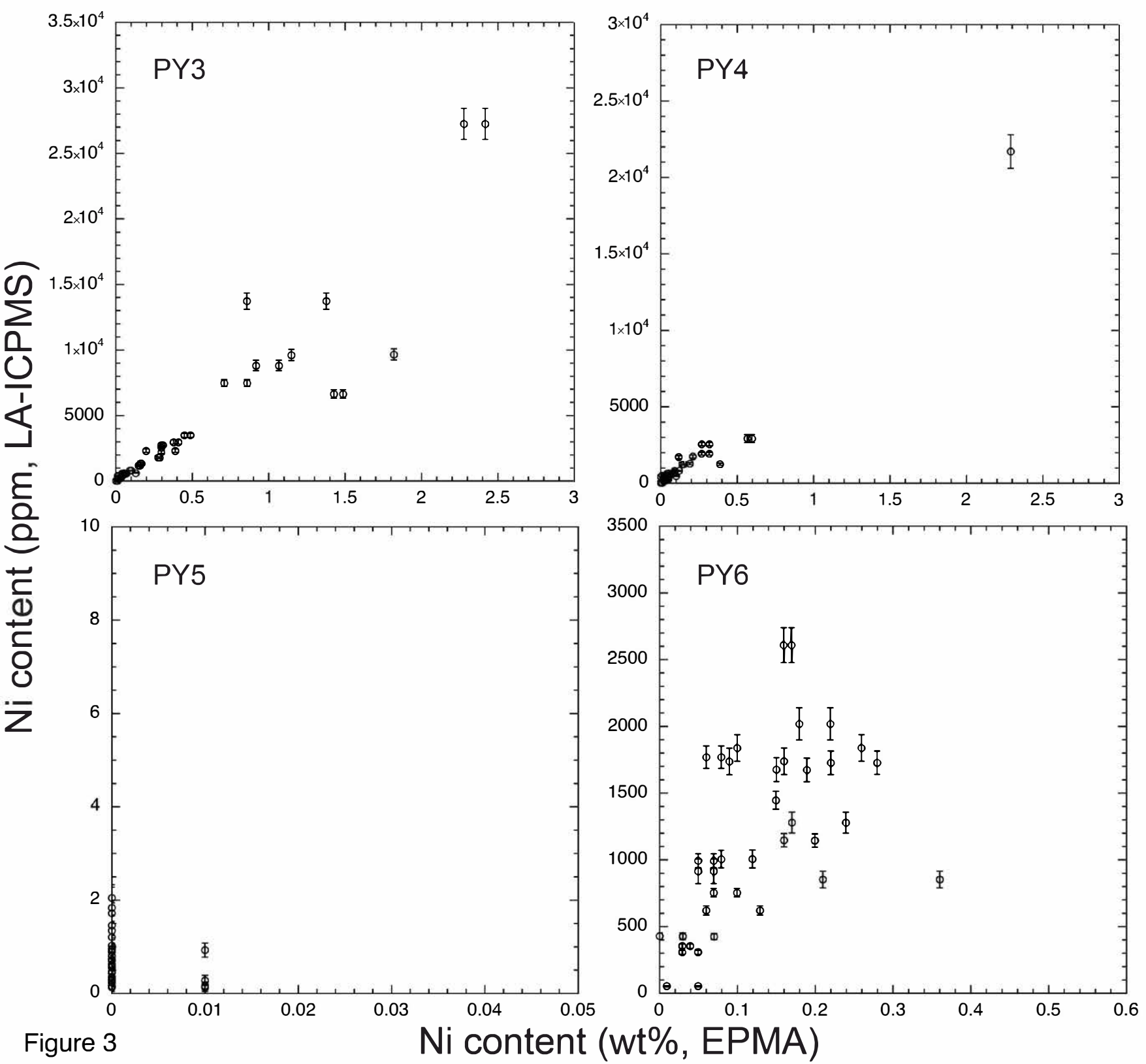

Figure 3

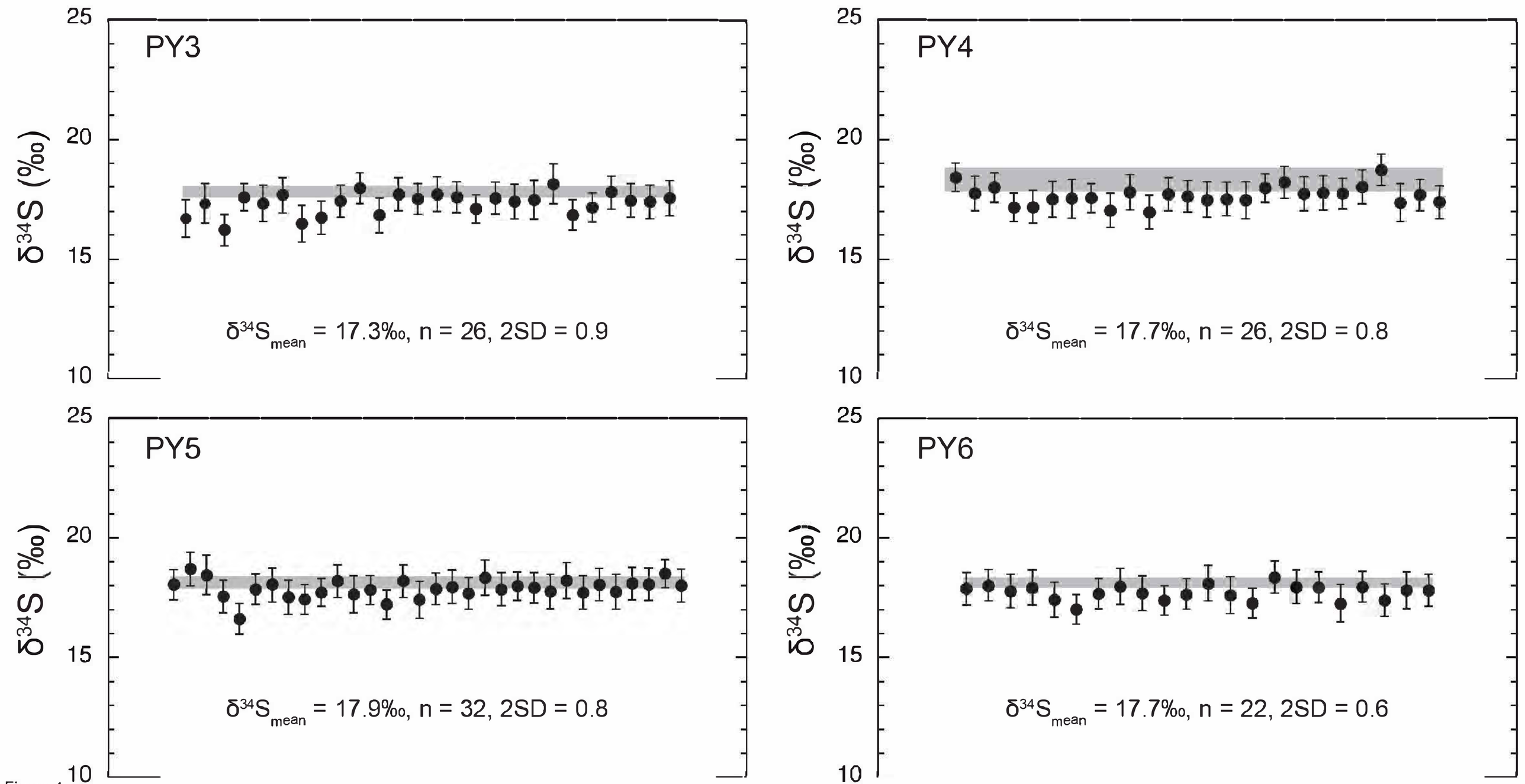
PY3
δ34S (‰)
δ34Smean = 17.3‰, n = 26, 2SD = 0.9
PY4
δ34S (‰)
δ34Smean = 17.7‰, n = 26, 2SD = 0.8
PY5
δ34S (‰)
δ34Smean = 17.9‰, n = 32, 2SD = 0.8
PY6
δ34S (‰)
δ34Smean = 17.7‰, n = 22, 2SD = 0.6
25
20
15
10

Figure 4

PY3

$\delta^{34}S$ (‰)

Ni con. (ppm)

17.1
3550

17.6
2580

17.6
2780

17.7
1815

200µm

16.7
9660

16.2
7510

17.6
13780

17.3
27300

200µm

PY4

17.5
296

17.5
341

17.6
450

200µm

18.2
1286

18.0
1750

17.7
2930

200µm

PY5

17.9
BDL

18.2
BDL

17.4
BDL

18.0
BDL

200µm

18.1
BDL

18.5
BDL

18.7
BDL

200µm

PY6

18.0
622

17.4
853

17.3
915

17.8
1280

200µm

17.9
1772

17.4
429

17.0
355

200µm

Figure 5

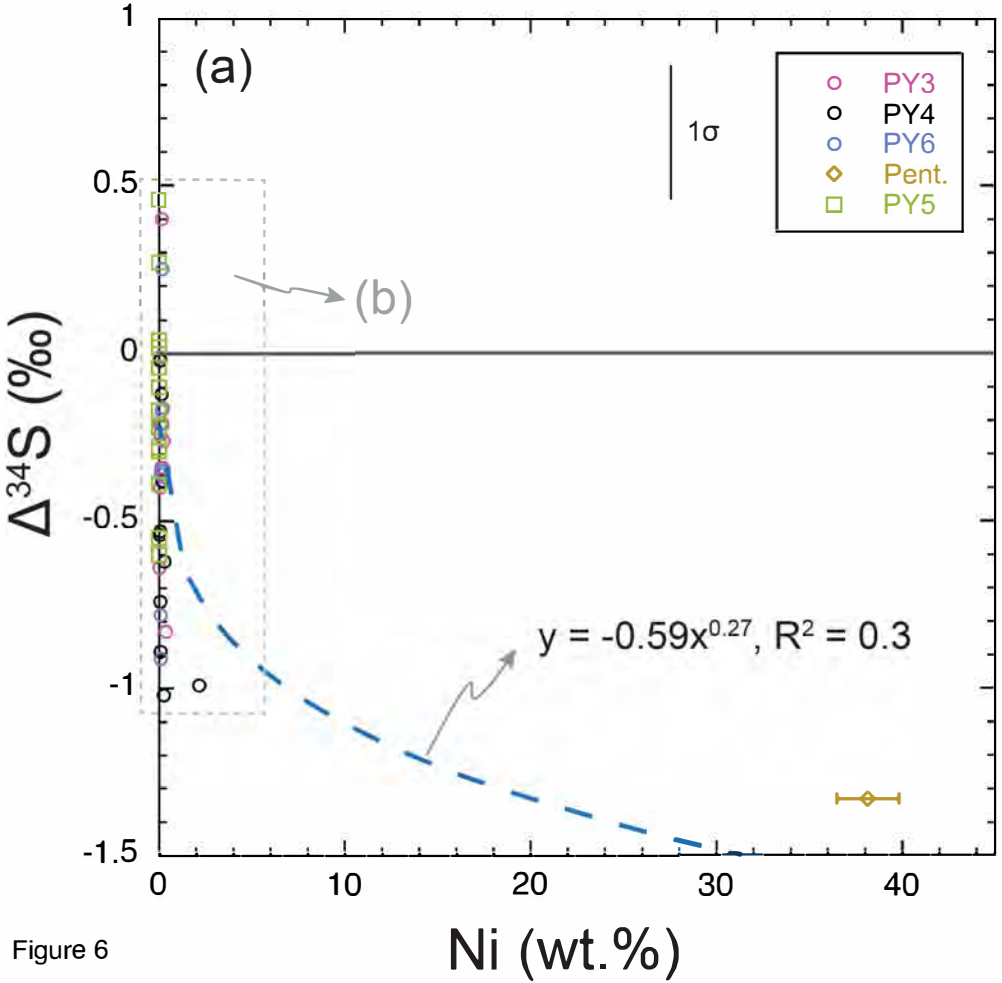
(a)
1σ
PY3
PY4
PY6
Pent.
PY5
(b)
y = -0.59x^0.27, R² = 0.3
Δ34S (‰)
Ni (wt.%)
1
0.5
0
-0.5
-1
-1.5
0
10
20
30
40

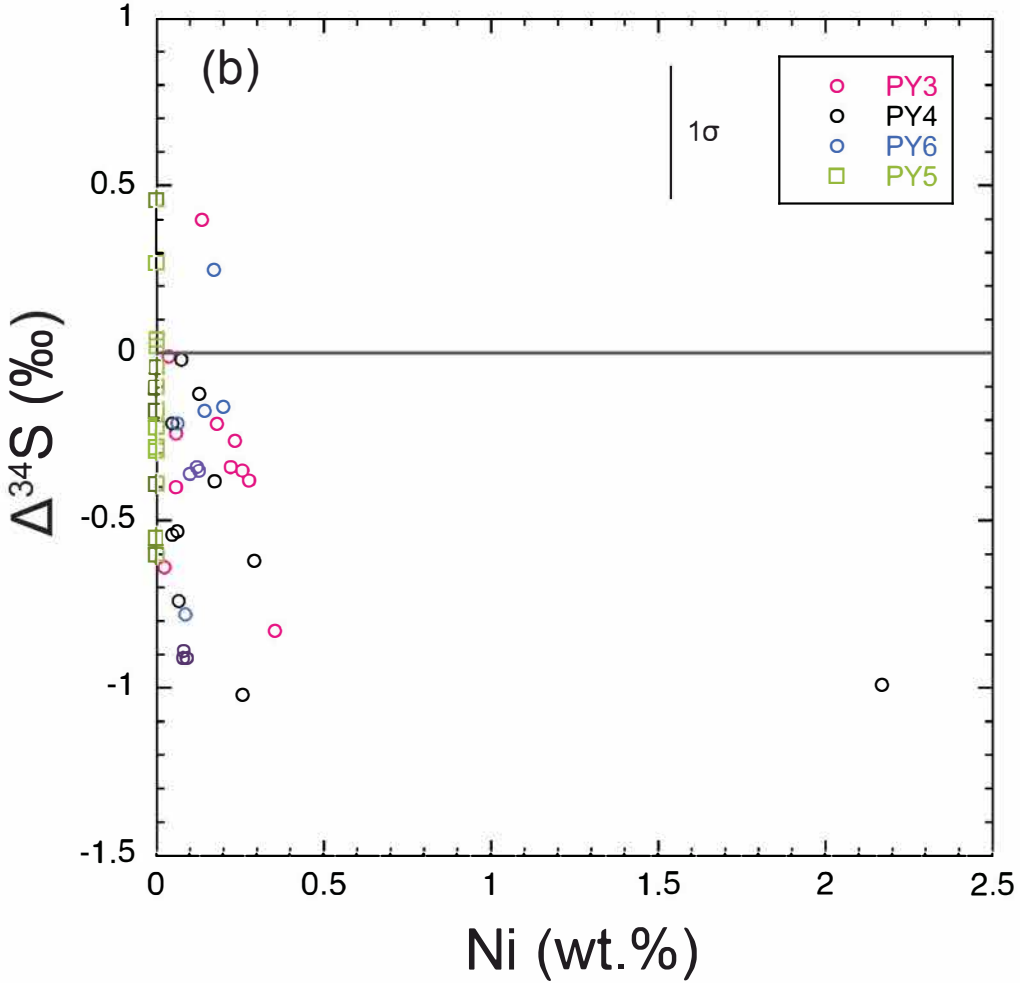
(b)
1σ
PY3
PY4
PY6
PY5
Δ34S (‰)
Ni (wt.%)
1
0.5
0
-0.5
-1
-1.5
0
0.5
1
1.5
2
2.5

Figure 6

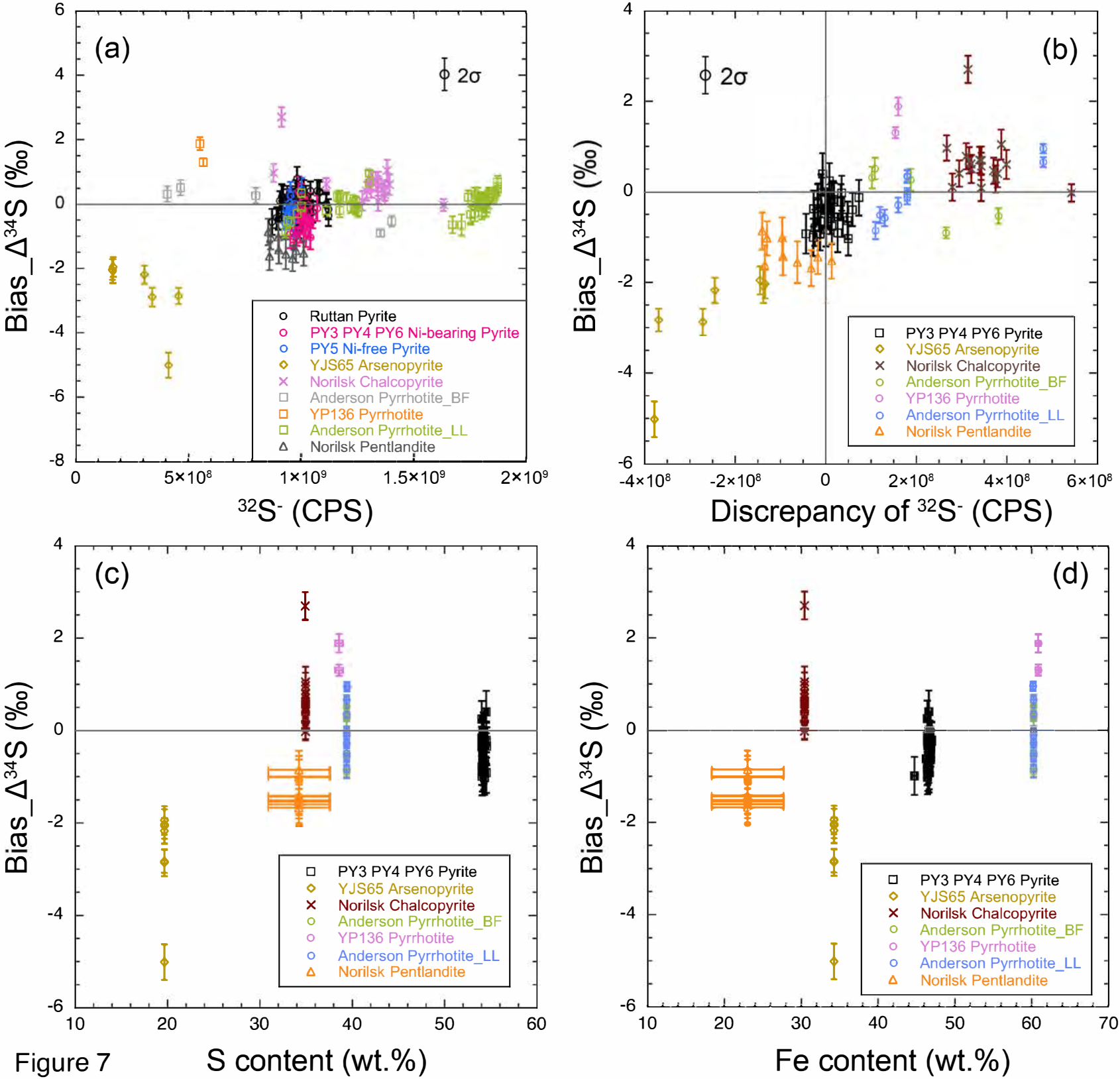
(a)
2σ
Bias_Δ34S (‰)
32S- (CPS)
Ruttan Pyrite
PY3 PY4 PY6 Ni-bearing Pyrite
PY5 Ni-free Pyrite
YJS65 Arsenopyrite
Norilsk Chalcopyrite
Anderson Pyrrhotite_BF
YP136 Pyrrhotite
Anderson Pyrrhotite_LL
Norilsk Pentlandite
(b)
2σ
Discrepancy of 32S- (CPS)
PY3 PY4 PY6 Pyrite
YJS65 Arsenopyrite
Norilsk Chalcopyrite
Anderson Pyrrhotite_BF
YP136 Pyrrhotite
Anderson Pyrrhotite_LL
Norilsk Pentlandite
(c)
S content (wt.%)
(d)
Fe content (wt.%)

Figure 7